ABSTRACT

Title of Document: LITHIUM AND ITS ISOTOPES AS A TRACER OF FLUID FLOW MECHANISMS IN THE CATALINA SCHIST MÉLANGE ZONE

Leigh Anne Roble, Master of Science, 2014

Directed By: Associate Professor, Dr. Sarah Penniston-Dorland, Department of Geology

Mélange zones are areas of highly mixed and deformed rock believed to form from shearing between subducting slab and peridotite mantle wedge. They have high –pressure/low-temperature mineral assemblages and contain a fine-grained matrix with centimeter to meter scale blocks surrounded by rinds, thought to represent a reaction zone between the block and matrix. These rinds are not well understood, but could be formed due to mechanical mixing, diffusion, or infiltration. Lithium is used to determine the role played by fluid-mediated processes in the Catalina Schist mélange zone because it is fluid mobile and has high diffusivity. Samples from amphibolite, lawsonite-blueschist, and lawsonite-albite facies were retrieved from the Catalina Schist subduction complex on Santa Catalina Island. Lithium isotopic

compositions and concentrations were determined using mass spectrometry techniques. One-dimensional diffusion models were applied to the data to determine the extent of the different mechanisms responsible for fluid transport throughout the subduction complex.

LITHIUM AND ITS ISOTOPES AS A TRACER OF FLUID FLOW MECHANISMS IN THE CATALINA SCHIST MÉLANGE ZONE

By

Leigh Anne Roble

Thesis submitted to the Faculty of the Graduate School of the
University of Maryland, College Park, in partial fulfillment
of the requirements for the degree of
Master of Science
2014

Advisory Committee:
Dr. Sarah Penniston-Dorland, Chair
Dr. Roberta Rudnick
Dr. James Farquhar

Acknowledgements

There are very many people that I have to thank for mentoring me and helping me along the way with this project. I would first like to profusely thank my advisor, Dr. Sarah Penniston-Dorland, for her constant support and guidance throughout this project. I would have absolutely not gotten through it without her insight and encouragement. From lab training and field work through data collection and interpretation, I could not have gotten here without her. I would like to acknowledge my committee members, Dr. Roberta Rudnick and Dr. James Farquhar, for being enthusiastic about being a part of my journey through my project and helping to guide me through the proposal defense up to my actual thesis defense.

I would also like to thank Dr. Igor Puchtel, Dr. Richard Ash, and Dr. Phil Piccoli for their support in the isotope geochemistry lab, plasma lab, and microprobe lab respectively. Their help and supervision within these facilities helped me to safely and efficiently prepare my samples and collect my data as well as to fully understand what it meant. I must also thank the other faculty that I have had courses with also have helped me to understand what it is to be a true research scientist, and how to look at a problem in multiple creative ways in order to try and solve it.

I would like to thank all the other graduate students at UMD, and specifically Miriam, Anna, Nick, Nívea, Emily, and Julia, for helping to answer questions I've had throughout my time at the university and making my time here tolerable.

Finally, I would like to thank all of my family and friends, most importantly my father and fiancé, David, for being there for me through it all and allowing me to vent and seek support when I didn't think I would make it through to the end.

Table of Contents

List of Tables

List of Figures

Chapter 1: Introduction

Subduction zones are tectonically active convergent margins where dense, mafic oceanic crust is forced beneath more buoyant continental crust. During subduction, the subducting slab carries mafic rocks, lithospheric mantle, and compacted sediments deep into the subduction zone. Studies of subduction-related metamorphic rocks shed light on processes within the subducting slab and at the slab-mantle interface that ultimately lead to the production of arc lavas. Detailed studies of these metamorphic suites reflect geochemical evolution near the slab-mantle interface and help characterize slab processes. Arc lavas are enriched in relatively fluid-mobile elements relative to melts produced by mantle melting, such as Rb, Ba, K, U, and Pb (Elliot, 2003; Morris and Ryan, 2003; Tatsumi, 2005). These enrichments can be attributed to several mechanisms, including sediment diapirs, relamination, melting from the subducting slab, or an influx of enriched fluids into the overlying mantle wedge from dehydration reactions in the slab (Bebout, 2007; Marschall and Schumacher, 2012).

Subduction-related mélange zones are areas of intensely mixed metamorphic rocks containing relatively high-pressure, low-temperature mineral assemblages. Mélange zones are thought to form at the interface between the subducting slab and the mantle, and are composed of heterogeneously deformed oceanic crust and sediments mixed in with variably hydrated and metasomatized ultramafic rocks of the mantle wedge. Deformation, fluid flow, chemical exchange, and partial melting contribute to the formation of mélange zones. Evidence suggests that rocks caught in

these zones experienced prograde metamorphic reactions, mechanical mixing, and metamorphic fluid flow (Bebout and Barton, 2002). Metamorphic fluid flow transfers trace elements through the subducting slab and mélange and likely into the overlying mantle wedge. This metamorphic fluid allows for mass transport across large distances and is associated with features such as veins and chemical and isotopic alteration of rocks along the flow path.

Mélange zones are common in exposed subduction zone metamorphic complexes and are typically made up of heavily mixed and deformed metamorphic rock with blocks, which can be up to hundreds of meters in scale. These blocks are composed of metasedimentary, metamafic, and metaultramafic rocks surrounded by a finer grained matrix. The blocks in many instances are surrounded by a reaction rind. A reaction rind is typically mineralogically and geochemically distinct from the block that it surrounds. Rinds are thought to form by fluid-mediated exchange reactions between the block and surrounding matrix (Sorensen and Barton, 1987; Sorensen and Grossman, 1989; Penniston-Dorland et al., 2012a). These reaction rinds can be several centimeters in thickness and provide information about fluid flow regimes that were present in the subduction zone and surrounding region.

Lithium, a fluid-mobile alkali metal, is a useful tracer of fluid-rock interactions (Brenan et al., 1998). There are two isotopes of lithium: ^{6}Li and ^{7}Li. When substituting into octahedral sites in minerals (e.g., garnets, micas (phengite and muscovite), and pyroxenes (spodumene); Wunder et al., 2006, 2007, 2011), ^{7}Li preferentially partitions into the fluid, while ^{6}Li partitions into the solid (Brenan et al., 1998; Caciagli et al., 2011; Ottolini et al., 2009). The opposite sense of partitioning

relative to fluids occurs when the lithium substitutes into tetrahedral sites in minerals such as staurolite (Wunder et al., 2007; 2011). Lithium fractionation can be up to 60 per mil, ‰, in terrestrial systems (Tomascak et al., 2004), and there is a mass difference of about 15% between these two isotopes (Hoefs et al., 1997). The large mass difference leads to a significant difference of diffusivity between the two isotopes, leading to fractionation during diffusion (Richter et al., 2003).

Lithium occurs in ppm concentrations in the upper mantle. The typical range of lithium concentration in mid-ocean ridge basalts (MORB) is between 3 and 8 ppm (Tomascak, et al., 2008). Sedimentary rocks have a wide range of concentrations, ranging up to 79 ppm (Bouman et al., 2004; Chan et al., 2006; James et al., 1999). This contrast is what makes Li an ideal element to trace the interaction of sedimentary-derived fluids through mafic rocks.

The metamorphic facies represented in the Catalina Schist range from the high-grade amphibolite facies to the low-grade lawsonite-albite facies (Bebout and Barton, 2002). In the amphibolite facies region, there are garnet amphibolite blocks and ultramafic-serpentinite blocks (ranging from less than a meter to hundreds of meters in diameter) surrounded by a fine-grained mélange matrix intermediate in composition between mafic and ultramafic (Bebout and Barton, 2002). The garnet amphibolites are composed of garnet, clinopyroxene, amphibole, titanite, rutile, and apatite with minor plagioclase and quartz. The mélange matrix surrounding these blocks and rinds is made up of minerals such as talc, chlorite, anthophyllite, tremolite, hornblende, enstatite, zircon, and rutile (Bebout and Barton, 1989, 1993, 2002; Bebout, 1997; Bebout et al., 1999; Platt, 1975; Sorensen, 1988; Sorensen and Barton,

1987). Reaction rinds are commonly composed of minerals such as chlorite, tremolite, hornblende, anthophyllite, talc, and/or phlogopite.

The lawsonite-albite and lawsonite-blueschist facies contain metamafic blocks with a mafic rind and fine-grained mélange matrix that is mostly mafic in composition. The blocks are composed mostly of chlorite, albite, lawsonite, stilpnomelane, calcic-sodic to sodic amphiboles with intermittent white mica (Penniston-Dorland et al., 2012a). The mélange matrix enveloping the lawsonite-albite and lawsonite-blueschist blocks is composed of chlorite, albite, quartz, lawsonite, tremolite, talc, and white mica (Bebout, 1997 and Bebout et al., 1999). The reaction rinds surrounding the lower grade rocks are mostly composed of chlorite and tremolite (Bebout, 1997; Bebout et al., 1999; Sorensen and Grossman, 1989). These rinds are thought to represent a zone of mixing and diffusion between the low-grade blocks and mélange matrix (Sorensen and Grossman, 1989; Bebout, 2007; Penniston-Dorland et al., 2012a).

The bulk-rock composition of the amphibolite facies block rinds is different from the block cores. The rinds are enriched in elements such as Mg, Cr, Ni, Os, Ir, and Ru, which are higher in the matrix. These enrichments are attributed to mechanical mixing (Penniston-Dorland et al., 2012b).

There are also enrichments in the rind of another suite of elements, K, Ba, Na, U, and Li, which are not enriched in the mélange matrix. Elevated concentrations of lithium in the metamafic rocks of the Catalina Schist compared to their MORB protolith (Sorensen, 1986; 1988; Sorensen and Grossman, 1989), between 10 and 32 ppm (Penniston-Dorland et al;., 2012a) also suggests a different source for these

elements, such as a sedimentary source, dissolved into fluids (Sorensen and Grossman, 1989; Penniston-Dorland et al., 2012a).

The lithium concentration in the amphibolite blocks ranges between 10 and 16 ppm, while the rinds have between 17 and 19 ppm lithium. The rind δ^7Li composition ranges from -1.1 to +0.3‰ compared to garnet amphibolite blocks, ranging from -5.5 to -0.3‰ (Penniston-Dorland et al., 2012a). The range of lithium concentration in MORB and altered MORB (the likely protolith of the amphibolite) for most samples falls between 3 and 10 ppm with δ^7Li between -2 and 14‰ (Bouman et al., 2004; Brenan et al., 1998; Chan et al., 1992, 2002, 2006; Jeffcoate et al., 2007; Teng et al., 2008; Tomascak et al., 2008). The only reported δ^7Li values for mantle rocks that are less than -2‰ are measured in mantle xenoliths (Tang et al., 2012). A possible mechanism for producing light δ^7Li values is diffusive fractionation of lithium. This diffusive fractionation is driven by the differences in diffusivity between ^{6}Li and ^{7}Li because of their mass difference, with ^{6}Li diffusing more rapidly than ^{7}Li.

The results for Catalina Schist amphibolites and reaction rinds have led to several questions. This study addresses some specific questions, such as 1) why are the rinds enriched in Li relative to the blocks or the mélange matrix, 2) why do the garnet amphibolite blocks have such low δ^7Li and where did the light Li composition originate, and 3) what is the source of the Li in the subduction zone. This study also addresses a more general question: what can measurements of Li in rinds tell us about processes such as fluid infiltration and diffusion?

Chapter 2: Geologic and Geochemical Background

Section 2.1: Geologic Background

The Catalina Schist is a Cretaceous subduction-related metamorphic complex located on Santa Catalina Island off the coast of California near Los Angeles, shown in Figure 1.

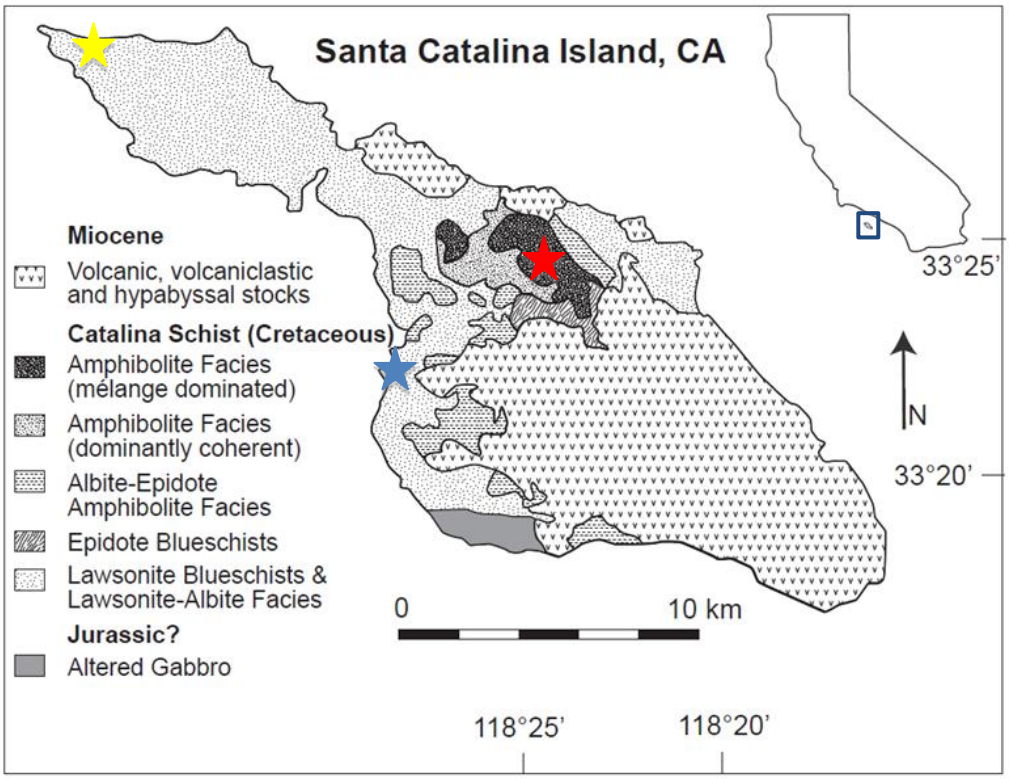

Figure 1: Geologic map of Santa Catalina Island (Grove and Bebout, 1995); top right corner shows outline of California, with blue square representing inset of Santa Catalina. Stars indicate sample localities (red: amphibolite facies, blue: lawsonite-blueschist facies, yellow: lawsonite-albite facies).

The metamorphic rocks of the Catalina Schist have protoliths ranging from sedimentary to mafic and ultramafic, leading to metasedimentary, metamafic and metaultramafic rocks throughout the Catalina Schist (Bebout and Barton, 1989). The

peak metamorphic conditions of the rocks on the island are estimated to have been between 0.5 GPa and 1.2 GPa and 350°C-750°C (Bebout and Barton, 1989, 1993; Sorensen and Barton, 1987). The mélange matrix minerals record peak metamorphic recrystallization at similar conditions as those for most blocks throughout the mélange (Bebout 1993). The range of metamorphic facies exposed in the Catalina Schist includes lawsonite-albite, lawsonite-blueschist, epidote-blueschist, epidote-amphibolite, and amphibolite facies. Estimates of the pressure and temperature ranges for each facies can be found in the facies diagram in Figure 2.

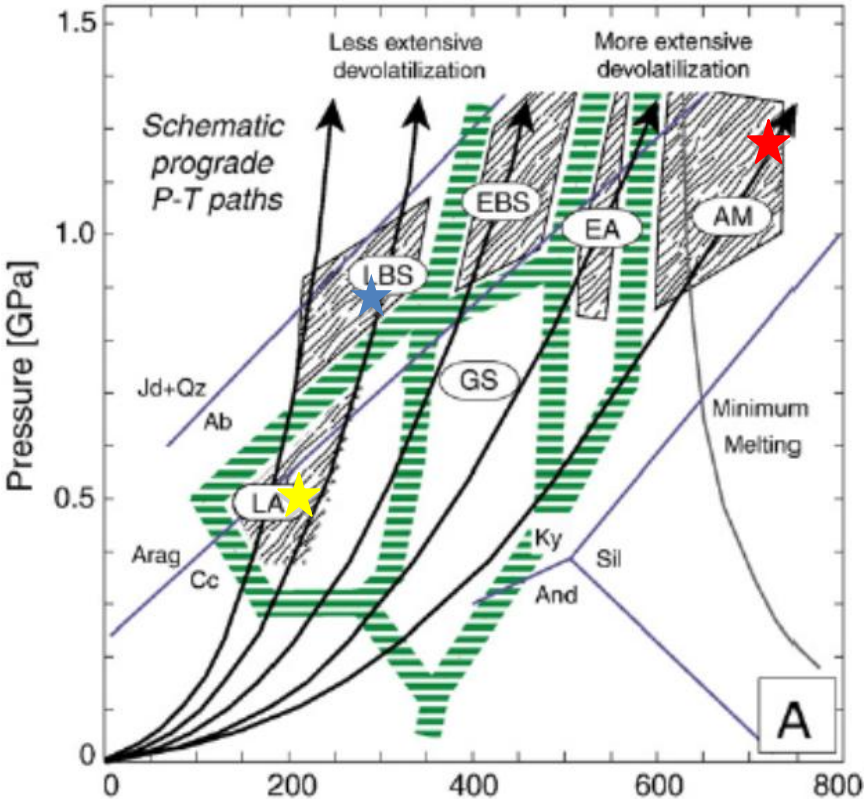

Figure 2: Facies diagram with relevant metamorphic facies of the Catalina Schist (Bebout, 2007); stars indicate metamorphic facies of samples collected for this study, with the same color scheme as Figure 1. LA-lawsonite-albite, LBS-lawsonite-blueschist, GS-greenschist, EBS-epidote-blueschist, EA-epidote-amphibolie, AM-amphibolite, Ky, kyanite, Sil-silliminate, And-andalusite, Jd-jadeite, Qz-quartz, Ab-albite, Arag-aragonite, Cc-calcite.

The structural history of the area is complex. There is an inverted metamorphic gradient in which the highest grade metamorphic rocks are on top structurally with the lowest grade metamorphic rocks on the structural bottom (Grove et al., 2008). This may reflect a thermal regime that started during subduction, and then was uplifted during active margin conditions (Grove et al., 2008).

Detrital zircon U-Pb ages suggest a maximum depositional age of 122 Ma for the amphibolite facies metasedimentary rocks of the Catalina Schist (Grove et al., 2008) and an age between 97 and 95 Ma for lawsonite-blueschist facies (Grove et al., 2008) with approximately 20 million years of accretion and subduction taking place during the early Cretaceous (Grove et al., 2008). Garnet Lu-Hf data yield ages of 114.5±6 Ma (Anczkiewicz et al., 2004), directly dating the age of peak amphibolite facies metamorphism in the mid-Cretaceous. K-Ar dating amphiboles, micas, pyroxene, and whole rocks yield metamorphic ages from 98-112 Ma (Suppe and Armstrong, 1972).

Metaultramafic and metamafic rocks are most abundant in amphibolite facies while the blueschist facies rocks are almost 70% metasedimentary (Bebout and Barton, 1993). The metasedimentary rocks consist of metamorphosed pelagic, pelitic and siliceous sediments, as well as metagraywackes and metaconglomerates (Bebout and Barton, 1993). The sedimentary, mafic, and ultramafic rocks in the Catalina Schist metamorphosed over a wide P-T range record evidence for compositional changes via mechanical mixing, diffusion, and larger-scale fluid-mediated transfer processes (Bebout and Barton, 1989; Bebout, 1991; Bebout and Barton, 1993; Bebout and Barton, 2002; Penniston-Dorland et al., 2012a; b).

The metamafic lawsonite-albite and lawsonite-blueschist facies rocks contain chlorite, albite, lawsonite, stilpnomelane, calcic-sodic to sodic amphiboles and (<1%) white mica (Bebout and Barton, 2002). The amphibolite grade rock assemblages consist of minerals such as garnet, clinopyroxene, hornblende, clinozoisite, chlorite, and biotite (Penniston-Dorland, 2012a). The mélange matrix is highly variable in composition, but it is typically dominated by ultramafic components like serpentine, talc, fuchsite, calcic amphibole, anthophyllite, and enstatite (Bebout, 1997).

Metasomatism is abundant throughout the Catalina mélange zones. This is evidenced by abundant veins, uniform O, C, and H stable isotopic composition due to homogenization by fluid flow processes, and the presence of reaction rinds (Bebout, 1991; Bebout and Barton, 1993). The fluid source for metasomatism in these rocks is thought to be sedimentary based on calculated $\delta^{18}O$ of water +13±1‰ (Bebout and Barton, 1989). Nitrogen and lithium isotopes are also homogenized, but on a smaller scale, within each individual metamorphic grade (Bebout, 1997; Penniston-Dorland et al., 2012a).

Section 2.2: Geochemical Background

Understanding elemental behavior and fluid mobility during subduction zone metamorphism and within the mélange zone is important for further understanding how these elements diffuse, partition, and fractionate between minerals and fluids during subduction processes. Partition coefficients and fractionation factors describe an element's behavior during fluid-rock interactions.

2.2.1 Partitioning

The partition coefficient (*D*) is a ratio of concentrations of an element between two phases containing that element in equilibrium. It is calculated by:

Eqn 2.1 $$\boldsymbol{D = \frac{conc_x}{conc_y}}$$

where the $conc_x$ is the concentration of the element in phase *x*, and $conc_y$ is the concentration of the element in phase *y*. Partition coefficients can be described for a range of scenarios, such as between two mineral phases or between a mineral and a fluid.

During high-temperature mineral-fluid partitioning, lithium preferentially partitions into fluids. Experiments by Brenan et al. (1998a) determined the partition coefficients in a clinopyroxene- garnet-fluid system at fixed temperature and pressure conditions (2.0 GPa and 900°C). The experiments used 0.5 molar aqueous NaCl mixed with pure H_2O for the fluid composition. The average partition coefficients were determined to be 0.16 (±0.3[1]) for the clinopyroxene-fluid system and 0.83×10^{-1} (±0.016) for the garnet-fluid system. Experimentally determined values of the partition coefficient for Li were close to mineral-melt values of partition coefficients found in natural systems (Brenan et al., 1998a). The mineral-melt experiments were done between olivine-, clinopyroxene-, orthopyroxene-, and amphibole-melt systems at a range of temperatures (1000-1350°C) and pressures (1 atm and 1.0-1.5 GPa). The average partition coefficients for lithium were measured to be 0.18 (±0.02[2]), 0.20 (0.03), 0.20 (0.02), and 0.16 (0.02) for each mineral-melt system, respectively. Other studies calculated partition coefficients for mineral-melt systems of 0.2-0.43 for

[1] Reported 1σ uncertainty in parentheses following values for Brenan et al. 1998a.
[2] Reported 1σ uncertainty from Brenan et al. 1998b.

olivine (1 atm, 1150-1245°C), 0.11-0.18 for clinopyroxene (1 atm, 1150-1245°C) (Ryan, 1989), 0.124 for amphibole (1.5 GPa, 1092°C), 0.064 for phlogopite (1.5 GPa, 1092°C) (LaTourrette et al., 1995), and 0.22-0.24 for plagioclase (1 atm, 1150-1245°C) (Ryan, 1989). Later experiments done by Yakob et al. (2012) measured the lithium partition coefficient between olivine and diopside at 1.5 GPa and 700-1100°C, and found it to be 2.0 ±0.2 independent of temperature.

Li concentration data from high-pressure metamorphic rocks (from Syros, Greece) has been used to determine Li partitioning among coexisting mineral phases. In decreasing order of Li concentration, they are clinopyroxene, glaucophane, chlorite, phengite, paragonite, tourmaline, garnet, and clinozoisite (Marschall et al., 2006). The minerals with extremely low concentrations (down to ppb levels) of Li include calcic amphibole, talc, titanite, quartz, albite, lawsonite, and chloritoid (Marschall et al., 2006). Partition coefficients range between 23 to 56 for clinopyroxene-garnet and 16 to 57 for glaucophane-garnet systems.

One of the major points to come out of the Marschall et al. (2006) study was that lithium has the potential to stay in rocks during prograde, high-pressure metamorphism of altered oceanic crust (Marschall et al., 2006). At lower metamorphic grades, the lithium starts out in chlorite. Once glaucophane begins to form due to metamorphic reactions, the lithium partitions into the glaucophane. As the glaucophane changes to form clinopyroxene, the lithium moves into the increasing clinopyroxene population, and the rock becomes eclogite (Marschall et al., 2006).

2.2.2 Fractionation

The fractionation factor (α) describes how an element's isotopes fractionate between phases within a given system. This value is determined experimentally for mineral-mineral interactions and mineral-fluid interactions. It is calculated by:

Eqn 2.2 $$\boldsymbol{\alpha = \frac{R_a}{R_b}}$$

where the R_a is the heavy-to-light isotope ratio of an element in phase *a* and R_b is the heavy-to-light isotope ratio of the same element in phase *b*.

Lithium can be incorporated into different sites within mineral lattices. The type of mineral and the elements available can affect which site it preferentially occupies. Lithium is preferentially found in octahedral sites of silicate minerals, such as amphiboles, pyroxenes, and micas (Yamaji et al., 2001), substituting for Mg or Al (Wenger et al., 1991). In staurolite, lithium occupies the tetrahedral sites (Hawthorne et al., 1993) and lithium concentration tends to increase with increasing iron content (Dutrow et al., 1986). Within aqueous fluids, lithium can change coordination number and can range from 4-, 5-, to 6-coordination with oxygen atoms (Yamaji et al., 2001). This change in coordination plays an important role in isotopic fractionation of lithium (Yamaji et al., 2001) due to the stretching frequency of the lithium atoms changing.

The fractionation of lithium is typically due to ^{6}Li preferentially occupying the more highly coordinated site than ^{7}Li (Taylor and Urey, 1938; Oi et al., 1989). Li is frequently incorporated into octahedral sites and is complexed in fluids as $[Li(H_2O)_4]^+$ with four-fold coordination (Wunder et al., 2007). Experiments between lithium-staurolite and aqueous fluids enriched with LiCl or LiOH as well as lithium-

mica and enriched aqueous fluids were done to explore isotopic partitioning and mineral-fluid coordination during subduction processes. These experiments were run at 3.5 GPa with temperatures ranging between 670-880°C and at 2.0 GPa with temperatures ranging between 300-500°C. The ^{7}Li was found to weakly partition into lithium-staurolite with 4-fold Li coordination but strongly partitions into aqueous fluid and mica with 6-fold Li coordination (Wunder et al., 2007). This study also found that lithium isotope fractionation is temperature dependent, with isotope fractionation decreasing as temperature increases.

Another Wunder et al. study (2006) looked at lithium isotopic fractionation between clinopyroxene and fluid. Clinopyroxene is the most important lithium carrier in eclogites, so looking at this relationship is crucial for understanding the behavior of lithium in subduction zones. The experiments were run between clinopyroxene and Cl- and OH- bearing fluids between 500 and 900°C and at 2.0 GPa. It was found that the ^{7}Li preferentially fractionated into the fluid, and there was no significant difference in the isotopic fractionation due to the fluid composition or coordination. The study concluded that fluids derived from the dehydrated slab would be enriched with ^{7}Li and that the heterogeneity of lithium isotopes in subduction zones is due to hydration-dehydration reactions.

Eclogites from Trescolmen, Switzerland were measured by Zack et al. (2003) for δ^{7}Li compositions to determine the extent of isotopic fractionation during dehydration processes. The range of δ^{7}Li compositions of the samples was from -11 to +5‰ (Zack et al., 2003). These results were unusual due to the low δ^{7}Li values measured. Zack et al. (2003) drew the conclusion that subducted slabs are recycled

into the mantle with light lithium isotope compositions relative to MORB, and could potentially be sampled by different areas such as hotspots and arc lavas. Marschall et al. (2006) produced a model of lithium in subducted oceanic crust and measured more eclogite samples from multiple locations (e.g.: Trescolmen, Switzerland and Syros, Greece) to investigate the claims made by Zack et al. (2003). Marschall et al. (2006) found that only a ~3‰ or less difference in δ^7Li composition can be accounted for by dehydration based on modeling. The group also concluded that the range of δ^7Li compositions (-21.9-+6‰) must be due to kinetic fractionation of lithium.

Lynton et al. in 2005 found slightly different results for lithium isotopic fractionation at specific P-T conditions. This study looked at lithium fractionation between quartz, muscovite, and chlorine-bearing aqueous fluids between 400 and 500°C and 50 to 100 MPa pressure. The experiments showed that the quartz and muscovite undergo rapid changes in their lithium isotopic compositions due to diffusion from lithium-bearing fluid at 500°C and 60 to 100 MPa.

The Lynton et al.(2005) study was significant because it contained the first evidence of substantial, systematic fractionation in Li isotopic compositions among common minerals and an aqueous fluid at temperatures occurring during magmatic processes. This study had different results from others, such as Wunder et al. (2007), possibly because the experiments performed were diffusion experiments, where the lithium was introduced by hydrothermal reaction within the aqueous fluid. The incorporation mechanism for substituting lithium into mica and for isotopic fractionation within the mica was unclear. The isotopic fractionation observed could

have been transport-controlled because of the type of diffusion experiment, and therefore not due to equilibrium fractionation (Wunder et al., 2007).

2.2.3 Diffusion

The diffusion of the element depends on the mobility of the isotopes and the difference in chemical potential within a system, as well as along temperature gradients (Richter et al., 2003). Diffusion can result in a type of physical kinetic fractionation, where isotopes are fractionated due to mass transport within a single phase if the isotopes have significantly different diffusivities (Richter et al., 2003). Most significant kinetic isotope fractionations were once thought to mainly exist in liquids like water, but more recent experiments have demonstrated this for silicate melts (Davis et al., 1990).

The diffusivity of lithium has been found to be much greater than that of many other fluid-mobile elements (Richter et al., 2003), by between 2 and 3 orders of magnitude. This was determined by creating a diffusion couple between molten MORB and natural rhyolite. The experiments were run between 1350-1450°C and pressures of 1.2-1.3 GPa. Lithium was found to diffuse rapidly across the MORB/rhyolite boundary during six minutes of experimental run time while other elements (Na, Mg, Al, Si, K, Ca, and Fe) showed almost no diffusive movement across the couple in the same amount of time (Richter et al., 2003). The diffusion coefficient measured for lithium in this experiment was $6x10^{-5}$ cm^2s^{-1} and the diffusivity modeled based on SiO_2 content was two orders of magnitude greater than that of CaO, K_2O, and SiO_2 (Richter et al., 2003).

Chapter 3: Study Approach

Mafic blocks and reaction rinds of the Catalina Schist have been shown to have different Li concentrations and isotopic compositions from the MORB protolith (Penniston-Dorland et al., 2012a). Processes that alter lithium concentrations and isotope ratios during subduction metamorphism include mechanical mixing, diffusion within an intergranular medium, and infiltration of fluids by advection. These processes should result in different Li concentration and δ^7Li composition profiles across reaction rinds. Mechanical mixing creates a distinct chemical difference in lithium either at the contact between the block and mélange matrix or at the block-rind contact, and concentrations and isotopic compositions are expected to vary irregularly across the rind. Diffusion creates a profile in Li concentration and a predictable pattern of δ^7Li across the reaction rind and/or into the core of the block. Since lithium has a high diffusivity, the distance the lithium travels through the rocks would be much larger than for elements with lower diffusivity. Advection of Li by metamorphic fluids creates drastic contrast across the block-rind boundary and generates concentrations and isotopic compositions that are very different from any local materials. Local materials include mafic blocks and surrounding mélange matrix. Examples of theoretical lithium concentration profiles based on the different processes affecting fluid migration can be seen in the following figures.

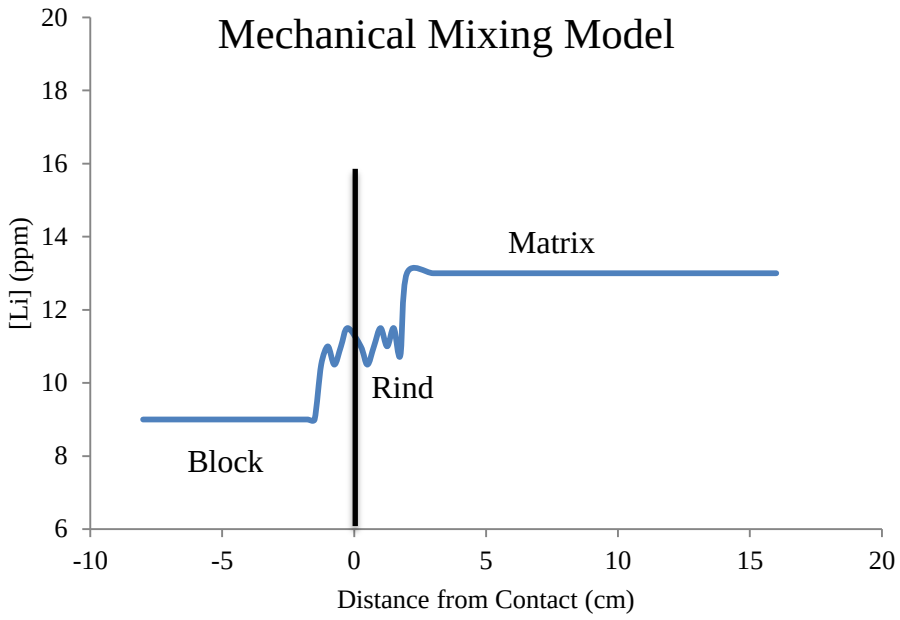

Figure 3: Mechanical mixing model example, where the core has lower initial lithium concentration and the matrix has higher initial lithium concentration. The concentration in the rind falls between the core and matrix values, and the process of mixing makes the rind concentration irregular in nature across the rind. Black line indicates location of original block/matrix contact.

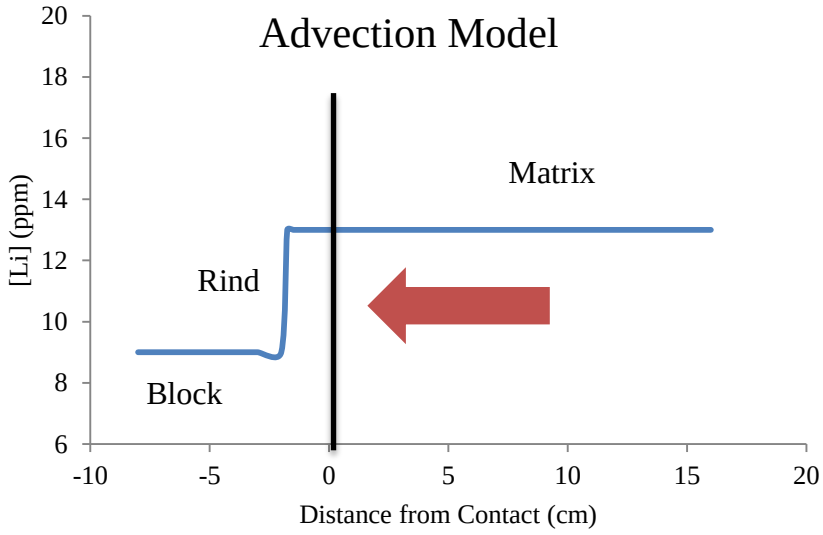

Figure 4: In this advection model, the matrix has high concentration relative to the core, and there is a sharp contrast between the two. The red arrow indicates fluid flow direction; as the fluid moves across the matrix surrounding the core, lithium concentration shifts its boundary through the rind into the core. Black line indicates location of original block/matrix contact.

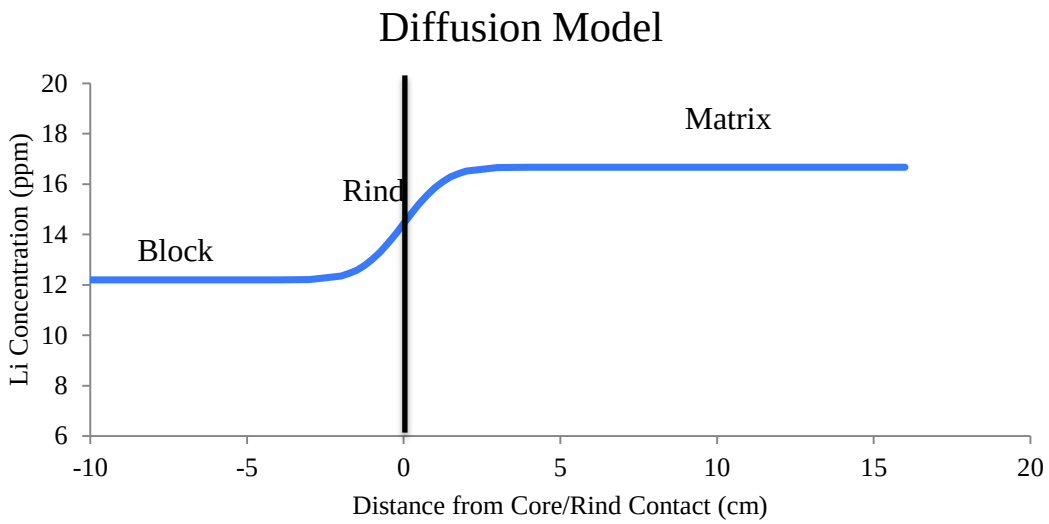

Figure 5: Diffusion model example. The concentration is gradational between the concentration in the matrix and the block. Black line represents original block/rind contact.

A combination of one or more of these processes could have occurred within the Catalina mélange zone. The concentration of the less fluid mobile elements are most likely to provide information about mechanical mixing, while variations in the fluid-mobile elements such as B, Be, Sr, and Li are most likely to provide information related to fluid movement throughout the system. Lithium data collected in this study were used to determine which of these processes: mechanical mixing, diffusion by fluids, or advection, was most influential in lithium transport through this system.

Section 3.1: Sampling Approach

The traverses across blocks, rinds and matrix were chosen on the basis of accessibility, context within the unit, and ability to collect a complete traverse. Five traverses were chosen from three metamorphic grades: amphibolite, lawsonite-blueschist, and lawsonite-albite facies. Two high grade amphibolite traverses spanned approximately 32.1 cm (A10-3 traverse) and 21.3 cm (A12-4 traverse) from garnet

amphibolite blocks across associated reaction rinds (Figure 6). The lower grade lawsonite-blueschist (14.0 cm in length for LB13-2) and lawsonite-albite traverses (11.0 cm in length for LA13-3 and 9.2 cm in length for LA13-2) sample across altered mafic blocks into the adjacent mélange matrix (Figures 7 and 8). When brought back to the lab, the blocks were cut perpendicular to the block-rind or block-matrix contact to expose the block (if not already exposed). The sample traverses were sliced parallel to the block boundary in 1-1.5 cm slices until the boundary was reached from each side. The sampling approach is illustrated in Figure 9.

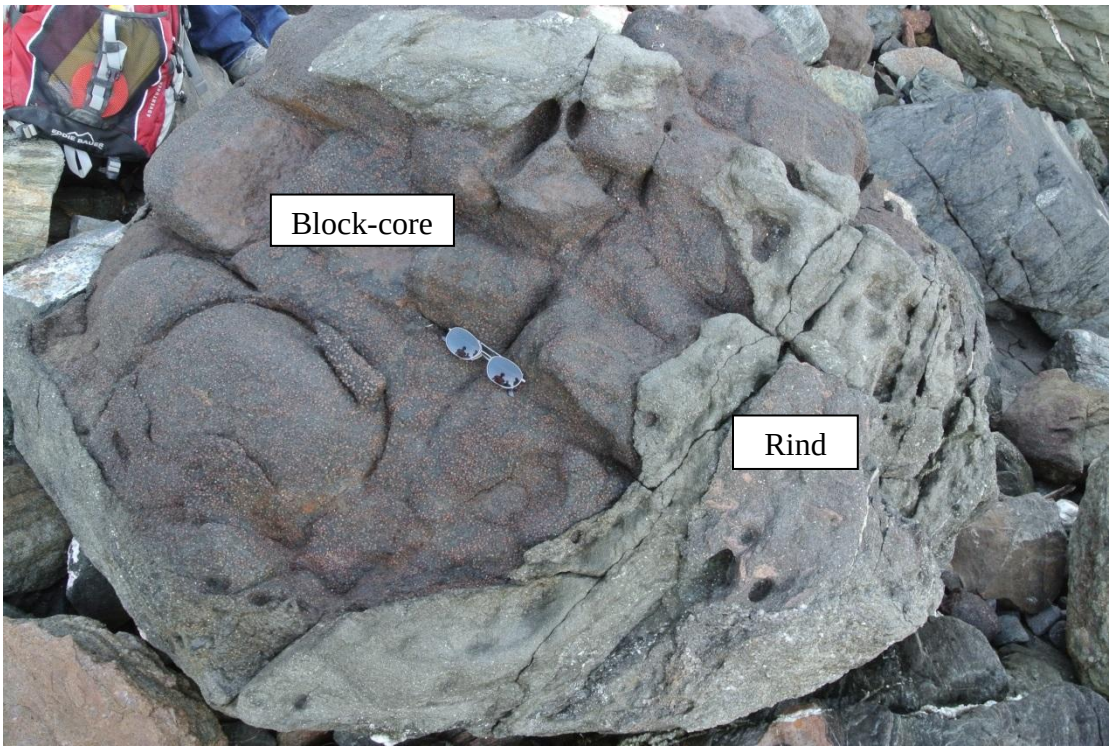

Figure 6: Amphibolite block in field with green reaction rind. Sunglasses included for scale. Block originated from field site represented by red star in Figure 1 (eroded down to beach on northern side of island from amphibolite facies locale).

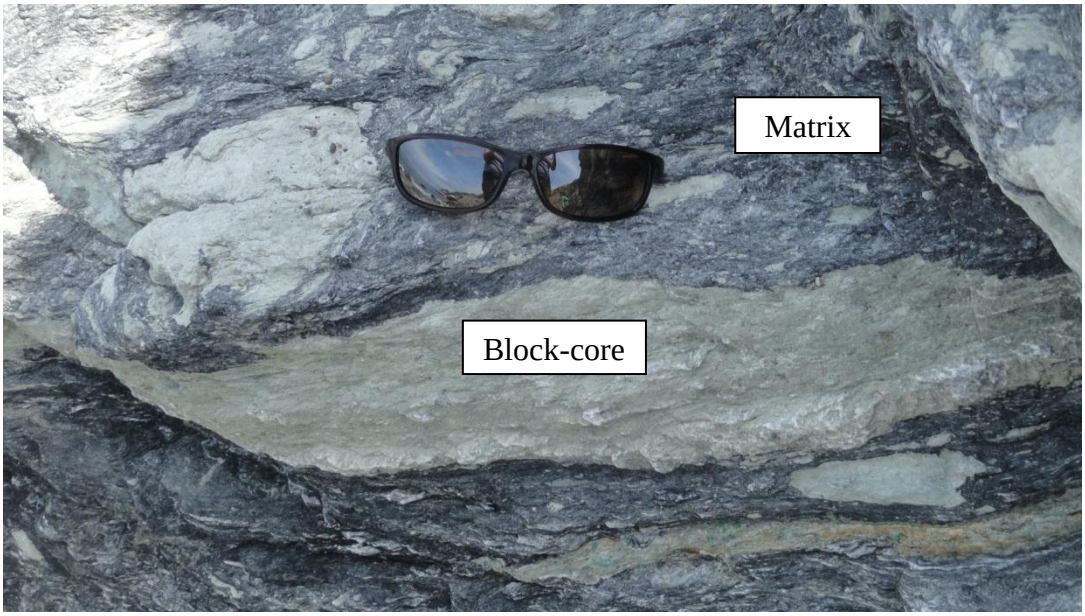

Figure 7: Lawsonite-albite facies altered green block with surrounding darker matrix. Sunglasses included for scale. Image taken at Starlight Beach (see yellow star, Figure 1).

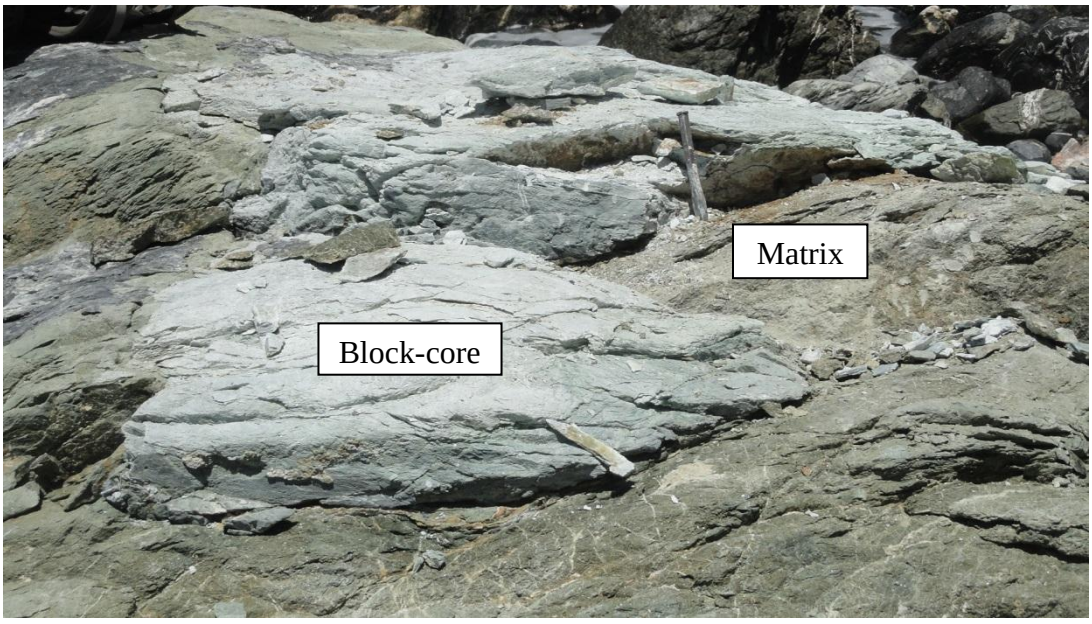

Figure 8: Lawsonite-blueschist facies field photograph with lighter colored block in the center and surrounding darker matrix. Chisel included for scale. Image taken at Little Harbor (see blue star, Figure 1).

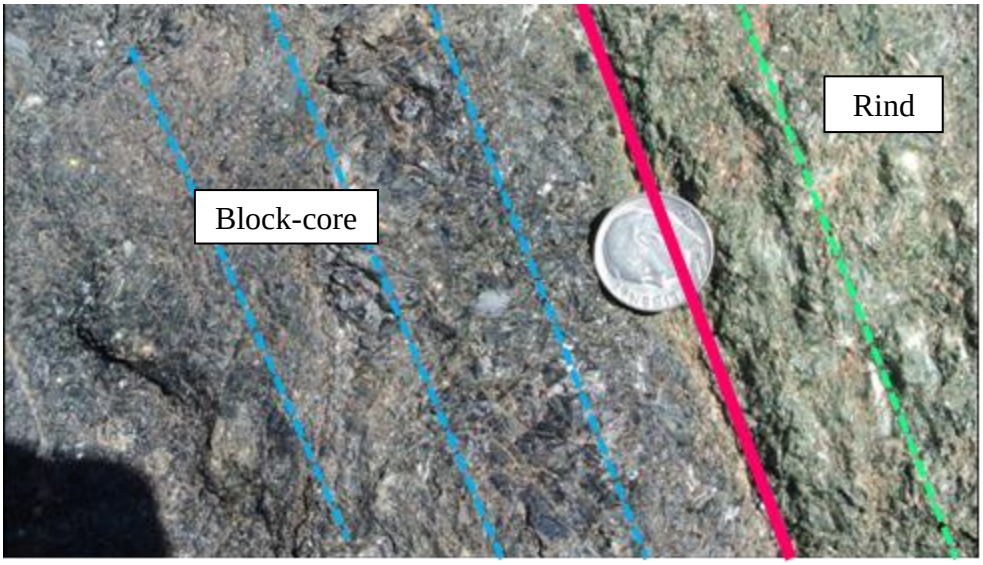

Figure 9: Example of an amphibolite block and rind contact with dashed lines indicating slicing pattern. Dime included for scale.

Chapter 4: Methodology

Section 4.1: Sample Preparation

Rocks were cut to fit in the mortar and pestle and to remove weathered parts. The pieces were then crushed with a steel mortar and pestle. They were powdered with the SPEX 8515 Shatterbox within a ceramic holder. Examples of traverses pre-sample slicing are shown in Figures 10 and 11.

Figure 10: LA12-3 traverse with arrow indicating block and matrix contact (block: bottom, matrix: top).

Figure 11: LB13-2 traverse sample, with arrows indicating contact between block and matrix (block: bottom, top: matrix).

Sample preparation for multi-collector inductively coupled plasma-mass spectrometry (MC-ICP-MS) was done according to the acid digestion method described in Teng et al. (2006). The powders were put into Savillex beakers on a hotplate at a temperature of 120°C. A sequence of acids was added, stepping from HF + HNO_3, to HNO_3, and then to HCl, with dry downs between each acid addition until the solution is clear. These solutions were put though three cation exchange columns to separate lithium (Teng et al., 2006). Several of the samples contained insoluble red crystals of rutile, which remained after the digestion process. These crystals were centrifuged to the bottom of the sample and were not processed through the column chemistry.

Section 4.2: Optical Microscopy

The thin sections from A12-4 were examined by transmitted and reflected light microscope. This was used to take images of the thin sections to create image maps. Amphibole grains were selected for the least amount of imperfections, such as fractures or discoloration, were selected and analyzed by the electron probe microanalyzer (EPMA) and laser ablation-inductively coupled plasma-mass spectrometer (LA-ICP-MS). An example of a selected amphibole grain can be seen in the following figure.

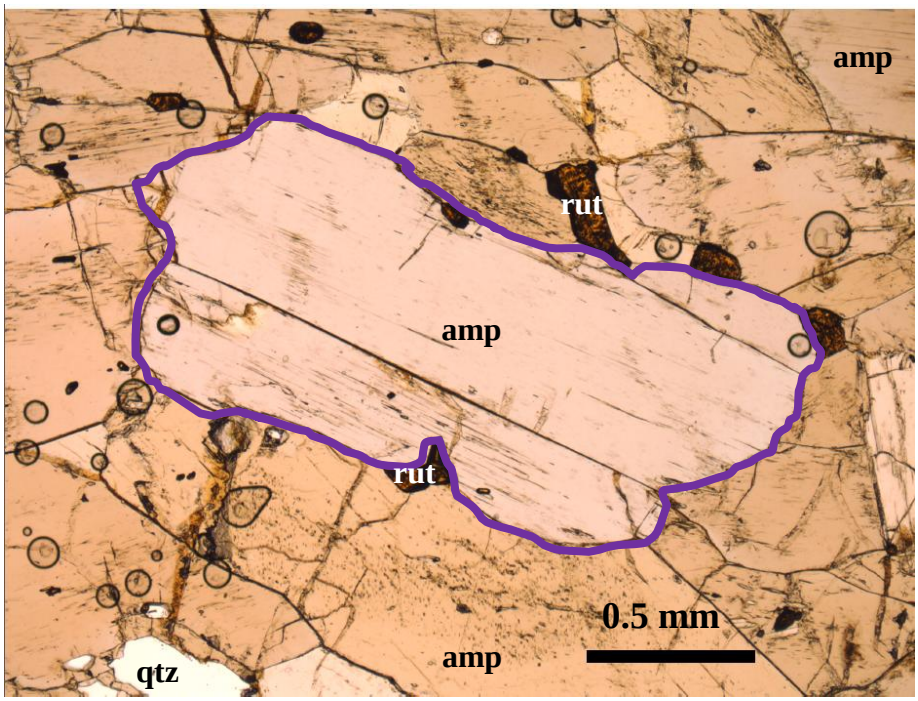

Figure 12: Thin section photomicrograph of sample A12-4A-C2 taken using plane-polarized light; amphibole grain outlined in center. Amp- amphibole, rut- rutile, qtz- quartz.

Section 4.3: Electron Probe Microanalyzer

The EPMA JXA-8900 SuperProbe used for this study is located in the Geology Department at the University of Maryland. It is a high resolution scanning

electron microscope (SEM) and a wave dispersive/energy dispersive (WD/ED) combined EPMA. The SEM was used to analyze the amphibole grains picked out by optical microscopy from the A12-4 thin sections to verify the mineralogy as well as measure the major-element compositions of the minerals. Thin sections were carbon coated for analysis. The accelerating voltage was 15 kV with a 20μm diameter beam and the current was set to 20nA. The primary standards used for analysis of the sample amphiboles were the Engel's amphibole and natural rhodonite with the Kakanui hornblende acting as secondary standard. The major-element composition of the Kakanui hornblende are reported Table 11 in the Appendix. The amphiboles were measured at a rim site and close to the core of the grain by the probe to see if there were significant changes or variability in lithium concentration at the mm scale due to diffusion processes. Raw data from the EPMA can be seen in Table 12 the Appendix.

Section 4.4: Mass Spectrometry

4.4.1 *Element 2* LA-ICP-MS

The amphiboles previously analyzed by EPMA were subsequently spot analyzed using the *Element 2* LA-ICP-MS at the University of Maryland for lithium. The thin sections were inserted into the instrument and the lithium concentration of the amphiboles was analyzed with the Nd-YAG 213 nm laser using a 55 μm spot size. The amphiboles were analyzed in the same spots as the EPMA analyses. The standards used for comparison with the sample amphiboles were the basalt standard reference material BCR-2G and homogenized glass standard NIST-610, with Ca analyzed as the internal standard.

The data were reduced using LAMTRACE software (Jackson, 2008), a spreadsheet-based LA-ICP-MS data reduction program. The standards are listed in Table 1 with the average Li concentration along with the accepted value for each standard. Uncertainty for LA-ICP-MS measurements of Li contents of amphiboles is ±12% (2σ) based on the standard deviation of measurements made on the standard BCR-2g (see Appendix). The standard deviation is a measure of how closely the majority of the data are to the mean of the data, and within 2σ, represents 95% of data. The smaller the standard deviation, the more alike the data are to each other. Complete standard data is listed in Table 12 in the Appendix.

Table 1: LA-ICP-MS Standard Values

Standard	*Average Total Li (ppm)*	*2σ Standard Deviation*
NIST-610 Accepted	468	-
NIST-610 Measured	463	4.68
BCR-2g Accepted	10	-
BCR-2g Measured	7.9	1.24

4.4.2 *Nu Plasma* MC-ICP-MS

Whole rock δ^7Li and [Li] were determined on the *Nu Plasma* MC-ICP-MS at the University of Maryland after column chemistry. The samples are put into 1ml of 2% HNO_3 and centrifuged to ensure no solids are introduced into the instrument. Standard-sample bracketing is used to correct for drift in the instrumental mass fractionation over time. The standard used is L-SVEC, and the accuracy is monitored using the in-house standard UMD-1 and international standard IRMM-016, helping to track long-term reproducibility in the lab. BHVO standards are also run through the entire digestion, column chromatography, and mass spectrometry in order to ensure the validity of the techniques used. The lithium concentration data collected for the

different traverses has a 10% error associated with it (Liu et al., 2010), and the δ^7Li compositions have 2σ uncertainty of ±1.2‰ based on repeat analyses of UMD-1 The δ^7Li and isotopic composition in ‰ was calculated by:

Eqn 4.1 $$\boldsymbol{\delta^7 Li = (\frac{(^7Li/^6Li)_{meas}}{(^7Li/^6Li)_{LSVEC}} - 1) \times 1000}$$

where the ratio for ^{7}Li to ^{6}Li of the sample is divided by the known ^{7}Li to ^{6}Li of the L-SVEC standard. The 2σ uncertainty on the standard with the highest uncertainty, UMD-1, is used to evaluate the uncertainty of sample measurements.

Measured values for UMD-1 and IRMM-016 δ^7Li are given in Tables 2 and 3. Measured values for the BHVO standards are given in Table 4 and Figure 15. The BHVO measurements are given along with other studies' results to demonstrate that the values measured for this study are within error of other lab measurements.

Table 2: Lab measured UMD-1 δ^7Li values.

	δ^7Li (‰)
UMD-1	54.6
	56.1
	55.2
	54.2
	55.9
	53.8
	55.6
	55.6
	55.0
	54.9
	55.2
	55.1
	54.9
	54.8
	55.0
	55.3
	55.0
	54.7
	54.4
	55.2
	54.9
	55.3
	53.9

	56.2
	55.4
	55.5
	54.7
Average	55.0
2σ Standard Deviation	1.18

Table 3: IRMM-016 concentration and lithium composition data.

	δ^7*Li (‰)*
IRMM-016	0.2
	0.2
	0.4
	0.1
	0.1
	0.3
	0.3
	0.4
	0.5
	0.8
	0.4
Average	0.3
2σ Standard Deviation	0.4

Table 4: BHVO standard values for [Li] and δ^7Li from various sources and current study.

BHVO-1	*Source*	δ^7*Li ‰*	*2σ error*	*[Li] ppm*	*1σ error*
	James and Palmer (2000)	5.8	1.6	-	-
	Pistiner and Henderson (2003)	5.1	0.9	4.0	-
	Chan and Frey (2003)	5.2	0.5	4.4	-
	Bryant et al. (2004)	6.1	1.0	-	-
	Rudnick et al. (2004)	4.3	1.0	-	-
	Bouman et al. (2004)	5.0	1.5	4.7	0.1
	Magna et al. (2004)	5.3	-	4.4	-
	Rosner et al. (2007)	4.7	0.2	-	-
	Aulbach et al. (2008)	4.5	1.0	-	-
	Halama et al. (2008)	4.4	0.7	-	-
	Maloney et al. (2008)	4.2	1.0	-	-
	Halama et al. (2009)	4.7	1.2	4.6	0.3
	Schuessler et al. (2009)	5.6	0.6	-	-
	Liu et al. (2010)	4.0	1.0	5.4	0.7
	Penniston-Dorland et al. (2010)	5.0	1.1	-	-
	Halama et al. (2011)	4.6	1.0	-	-
	Penniston-Dorland et al (2012)	4.4	1.1	4.3	1.2
	Liu et al. (2013)	4.6	1.1	4.1	0.6

	Liu et al. (in press)	4.6	1.0	4.1	0.3
	This Study	4.9	-	4.1	-
		4.8	-	3.4	-
	Average (This Study)	4.9	-	3.8	-
	Standard Deviation (This Study)	0.2	-	1.0	-

BHVO-2	*Source*	*δ^7Li ‰*	*2σ error*	*[Li] ppm*	*1σ error*
	Zack et al. (2003)	4.5	1.0	-	-
	Jeffcoate et al. (2004)	4.7	0.2	4.8	0.3
	Magna et al. (2004)	4.6	0.3	-	-
	Kasemann et al. (2005)	4.7	0.2	-	-
	Elliott et al. (2006)	4.7	0.3	-	-
	Magna et al. (2006a)	4.4	0.4	-	-
	Magna et al. (2006b)	4.5	0.2	-	-
	Jochum et al. (2006)	4.5	0.7	-	-
	Marschall et al. (2007)	4.8	0.2	-	-
	Magna et al. (2008)	4.5	0.3	4.6	-
	Penniston-Dorland et al. (2010)	4.3	1.2	-	-
	Gao & Casey (2011)	4.3	0.5	4.4	0.1
	Brant et al. (2012)	5.5	1.4	4.1	-
	Brant et al. (2012)	4.6	1.4	4.8	-
	Brant et al. (2012)	4.6	1.4	4.7	-
	Krienitz et al. (2012)	4.1	0.2	4.3	0.1
	Penniston-Dorland et al. (2012)	4.0	0.9	4.2	1.0
	Tian et al. (2012)	4.3	0.7	-	-
	Magna et al. (2014)	4.6	0.4	4.2	-
	Genske et al. (2014)	4.4	0.8	-	-
	This Study (Separate dissolutions)	4.4	-	5.6	-
		4.2	-	3.1	-
		3.5	-	4.8	-
		5.1	-	3.9	-
		4.3	-	4.0	-
	Average (This Study)	4.3	-	4.3	-
	Standard Deviation (This Study)	1.2	-	1.9	-

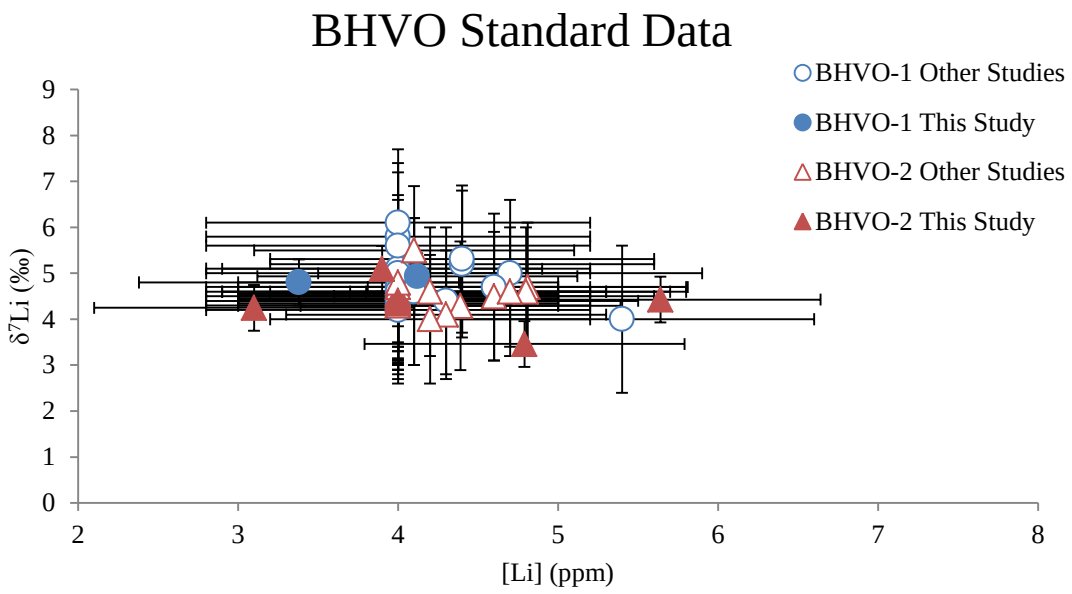

Figure 13: BHVO standard Li vs. δ7Li from this study compared to average values from studies listed in previous table; error bars represent 2σ uncertainties.

Chapter 5: Results

The traverses analyzed cover a wide range of metamorphic facies across Catalina Island and were chosen to give representative data for the different facies. The first traverses processed are from the amphibolite facies. These are A10-3 and A12-4, collected in 2010 and 2012, respectively (see red star in Figure 1). The traverses collected in 2013 focused on the lower grade rocks of Catalina. One traverse from the lawsonite-blueschist facies and two from the lawsonite-albite facies were processed. The lawsonite-blueschist traverse (LB13-2) was collected near Little Harbor (see blue star in Figure 1) and the two lawsonite-albite traverses (LA13-2 and LA13-3) were collected from Starlight Beach on the far west end of the island (see yellow star in Figure 1).

5.5.1 Mineralogy

The LA13-2 traverse is 9.2 cm long consisting of 3 matrix samples and 4 block samples with average slice thicknesses of 1 cm. The LA13-3 traverse is 11.0 cm long with 5 rind samples and 2 matrix samples with average slice thickness of 1cm. The LB13-2 traverse is 14.0 cm long containing 4 block/rind samples and 4 matrix samples with average slice thickness of 1cm. For all three of these traverse, some parts of the traverse were extremely weathered and broke into tiny pieces. These parts were not analyzed, leading to gaps in the traverses. Petrography was used to determine the mineralogy of samples in the LA13-2, LA13-3, and LB13-2 traverses. The whole of the LA13-2 traverse contained quartz, albite, chlorite, and muscovite, with minor talc, calcite, and lawsonite with minimal biotite. LA13-3 contained lawsonite, albite, and quartz with minor chlorite, biotite, and muscovite.

LB13-2 contained albite, calcic-sodic amphibole, chlorite, muscovite, calcite, and stilpnomelane with minor lawsonite. The major difference between lawsonite-albite and lawsonite-blueschist facies is the presence of amphibole in the lawsonite-blueschist facies rocks. Additionally there is less lawsonite present in the lawsonite-blueschist facies.

The A10-3 traverse is 32.1 cm long with 16 rind samples and 16 block samples with average slice thickness of 1cm. The A12-4 traverse is 21.3 cm long with 6 block samples and 7 rind samples with average slice thickness of 1.5cm. A10-3 and A12-4 are traverses originally analyzed by Gorman (2013) for highly siderophile elements (HSE). Mineral abundances were determined using EPMA at the University of Maryland for the amphibolite grade traverses, with 2642 points measured on the A10-3 block and 1847 points measured in the A10-3 rind (Gorman, 2013). For the A12-4 traverse, 2298 points were measured on the block and 2167 points were measured in the rind (Gorman, 2013). The modal mineral data for the A10-3 and A12-4 traverses can be seen in Table 5.

Table 5: Mineral modes expressed as volume percents for A10-3 and A12-4 traverses ±2σ standard deviation from Gorman (2013).

Traverse		*Hornblende*	*Garnet*	*Chlorite*	*Phengite*	*Rutile*	*Quartz*
A10-3	Block	78±2	12±1	5±1	4±0.8	1±0.6	-
	Rind	85±2	-	6±1	8±1	1±1	-
A12-4	Block	79±2	15±1	1.5±0.6	1±0.5	1.5±0.6	2±0.6
	Rind	82±2	-	7.7±1	2±0.6	0.5±0.3	7.8±1

The minerals in the amphibolite grade traverses show abrupt changes in mineralogy at the block-rind contact.

Amphiboles from the A12-4 traverse were analyzed by EPMA and LA-ICP-MS (see table 12 in Appendix). The MgO and SiO_2 content of the amphiboles increases as the traverse goes from the core to the rind, while the Al_2O_3 and FeO content decreases along the same trend. The average Al_2O_3 and FeO concentrations in the block cores are 14.4 and 12.7 wt.% respectively while in the rind, they are 12.9 and 10.2 wt.%, while the average MgO and SiO_2 concentrations in the core are 12.5 and 46.6 wt.% respectively and in the rind they are 14.8 and 44.9 wt.%. The amphiboles were classified as mostly tschermakite in the core, but predominately as magnesiohornblende in the rind.

Section 5.2: Li Concentration of Amphiboles

Total Li concentrations of amphibole grains were measured across three thin sections for the A12-4A traverse. The standards measured along with the samples were NIST-610 and BCR-2g. The average measured concentration for BCR2-g was 8 ppm Li, while the accepted value is 10 ppm Li. The average value measured for NIST-610 was 463 ppm, and the accepted value is 468 ppm. The lithium concentration values have a 2σ error of ±12% associated with it based on the more conservative calculated standard deviation of BCR-2g. The Li concentration data for amphiboles in the A12-4A traverse are represented in Figure 14 and Table 14 in the Appendix.

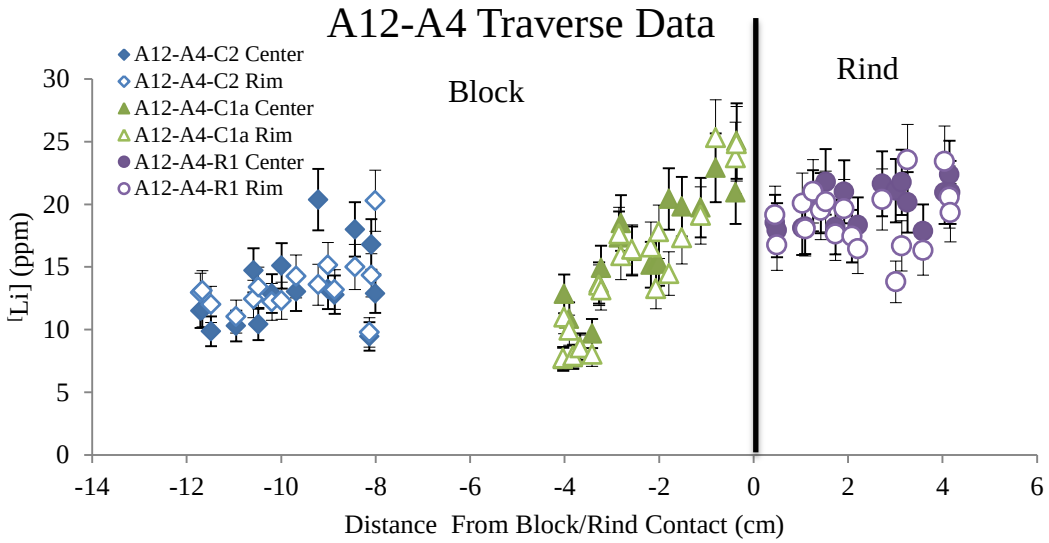

Figure 14: Li concentrations of amphibole grains as a function of distance across the A12-4A thin sections.

Amphiboles in the rind have an average concentration of 19 ppm and range from 14 to 24 ppm. Amphiboles in the block core away from the contact have an average concentration of 14 ppm and range from 9 to 20 ppm. The Li concentration of amphiboles in the block core near the contact shows an increase from ~10 ppm near the core to ~23 ppm near the rind.

Section 5.3: Whole-Rock Li Concentration and Isotopic Compositions

LA13-2 Traverse

The measured LA13-2 traverse whole-rock lithium concentrations and δ^7Li compositions can be seen in Table 6 and Figures 15 and 16.

Table 6: Lawsonite-albite traverse LA13-2 whole-rock Li concentration and δ^7Li composition data**.**

		Distance from Contact (cm)	*[Li] (ppm)*	*δ^7Li (‰)*
LA13-2	Block	4.7	97	2.2
		3.7	90	4.2
		2.7	116	4.8
		1.7	82	4.0
	Matrix	4.5	68	3.7

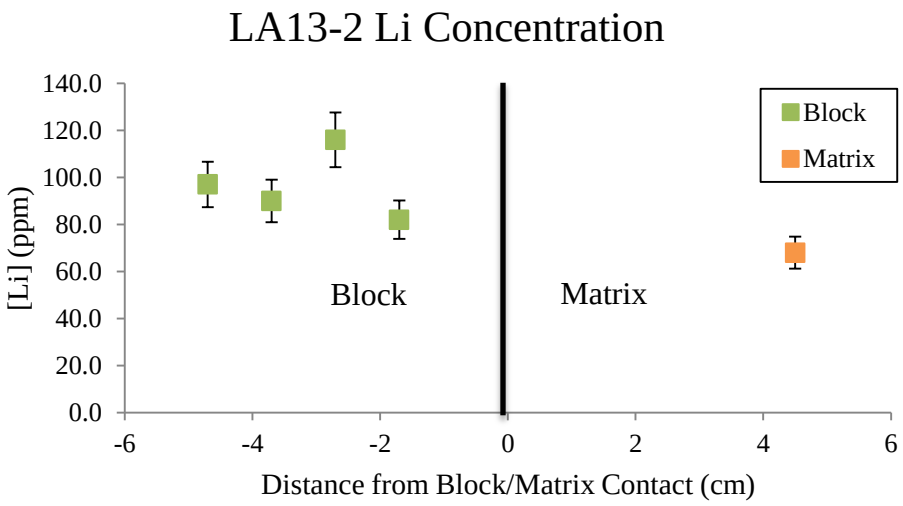

Figure 15: Li concentration in ppm for lawsonite-albite traverse LA13-2.

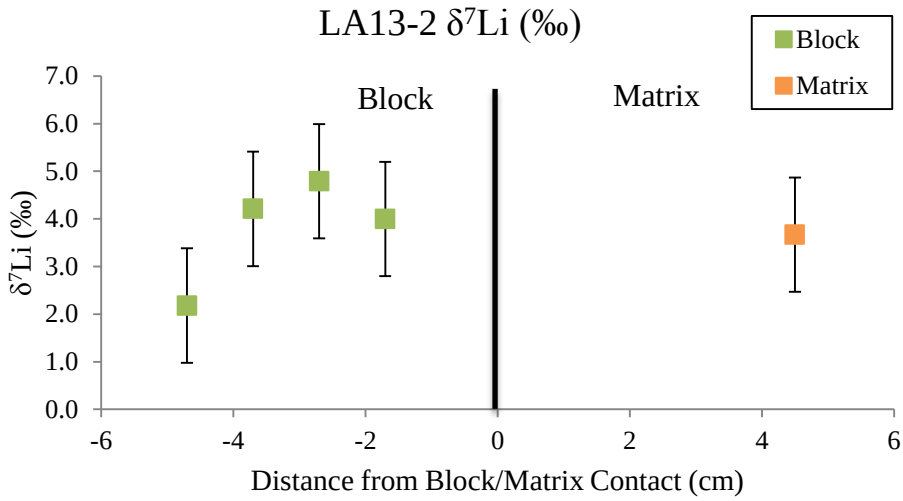

Figure 16: δ^7Li composition for lawsonite-albite traverse LA13-2.

These figures show that the block, for the most part, has a higher lithium concentration compared to the matrix. The concentration is 68 ppm in the matrix and ranges from 82 to 116 ppm in the block. The isotopic composition of the block and matrix overlap in composition. The δ^7Li is +3.7‰ in the matrix and ranges from +2.2‰ to +4.8‰ in the block.

LA13-3 Traverse

The measured LA13-3 traverse whole-rock lithium concentrations and δ^7Li compositions can be seen in Table 7 and Figures 17 and 18.

Table 7: Lawsonite-albite traverse LA13-3 Li concentration and δ^7Li composition data.

		Distance from Contact (cm)	*[Li] (ppm)*	*δ^7Li (‰)*
LA13-3	Block	5.7	44	2.3
		4.7	52	5.5
		3.7	53	2.0
		2.7	63	4.2
		1.2	70	4.3
	Matrix	2.5	9	1.5

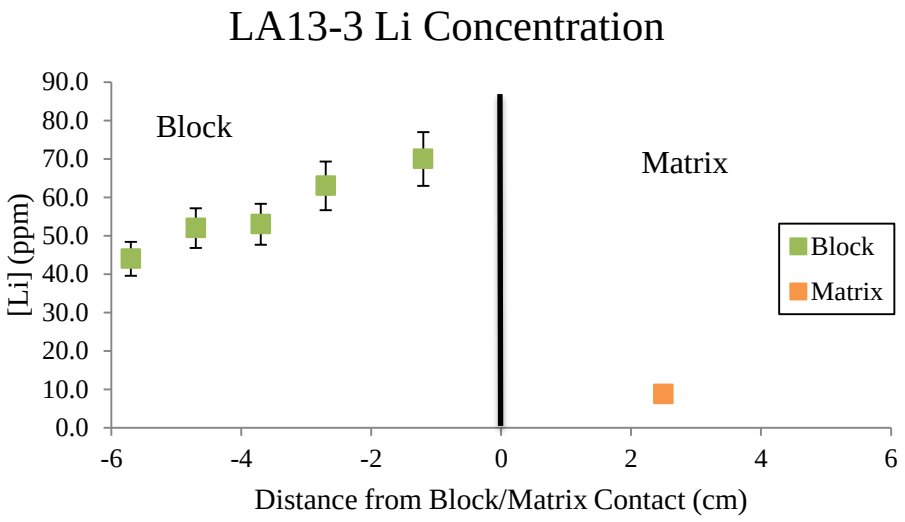

Figure 17: Li concentration for lawsonite-albite traverse LA13-3.

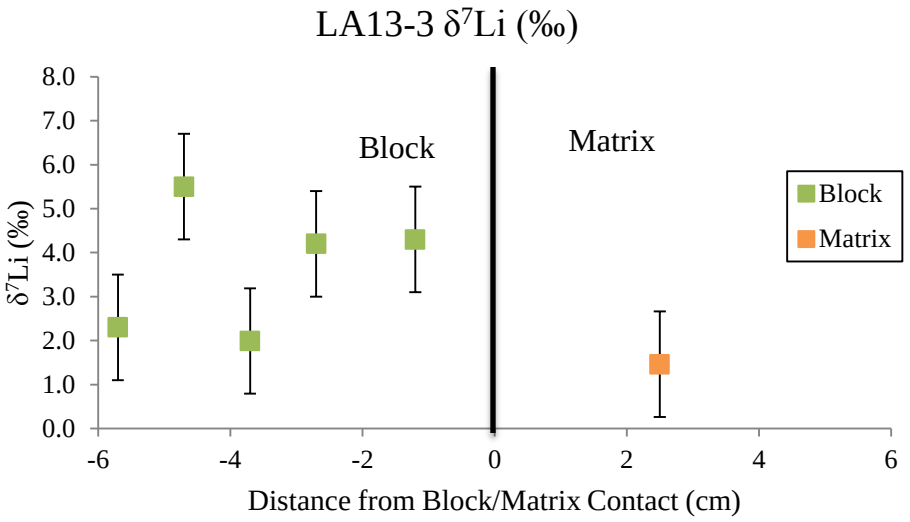

Figure 18: δ^7Li composition for lawsonite-albite traverse LA13-3.

Lithium concentrations in the block are much higher than the concentration in the matrix. The lithium concentration is 9 ppm in the matrix and ranges from 44 to 70 ppm in the block. The isotopic composition of the matrix slightly overlaps with the block. The δ^7Li is +1.5‰ in the matrix and ranges from +2.0 to +5.5‰ in the block.

LB13-2 Traverse

The measured LB13-2 traverse whole-rock lithium concentrations and δ^7Li compositions can be seen in Table 8 and Figures 19 and 20.

Table 8: Lawsonite-blueschist traverse LB13-2 Li concentration and δ^7Li composition data.

		Distance from Contact (cm)	*[Li] (ppm)*	*δ^7Li (‰)*
LB13-2	Block	4.8	72	4.6
		3.8	44	5.3
		2.8	48	1.4
		1.8	44	3.4
	Matrix	1.5	8	-0.4
		2.5	11	-0.4
	Replicate	2.5	11	-0.8
		3.5	10	0.0
		4.5	10	-1.1

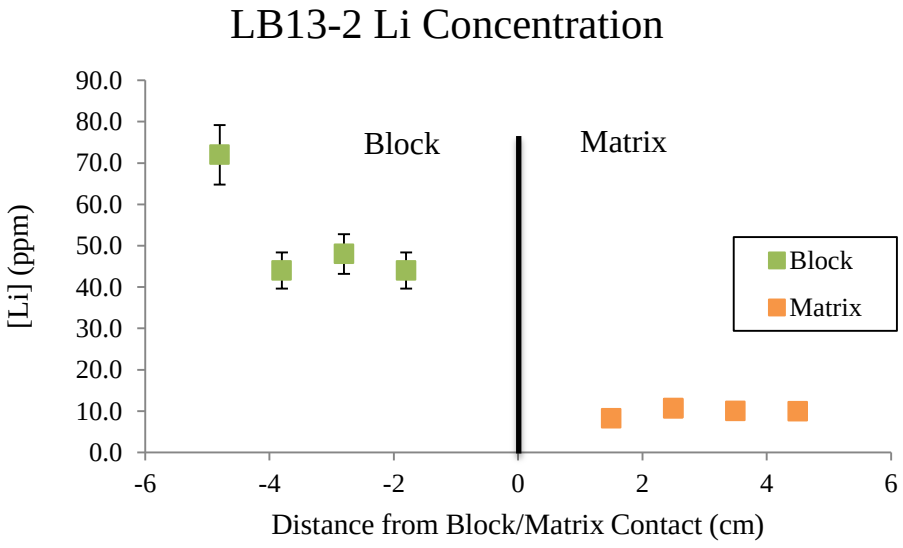

Figure 19: Li concentration for lawsonite-blueschist traverse LB13-2.

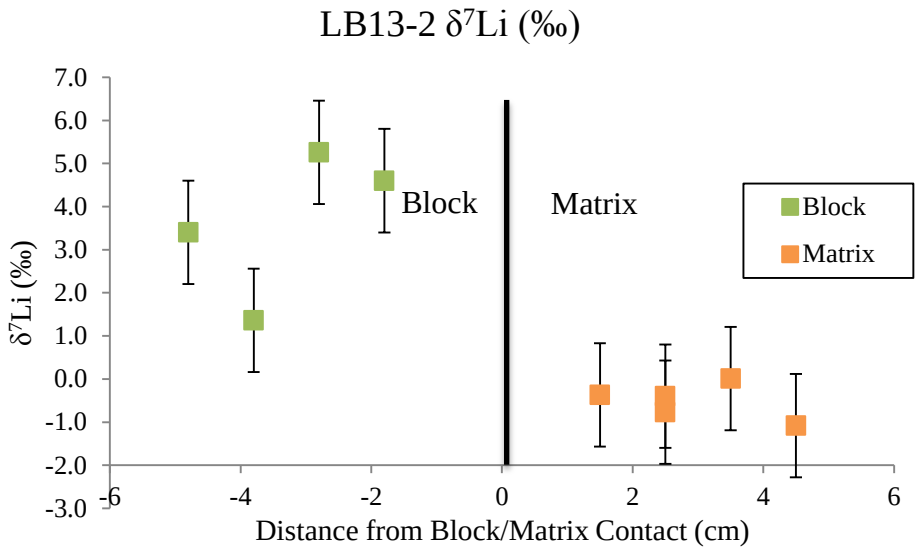

Figure 20: δ^7Li composition for lawsonite-blueschist traverse LB13-2.

Like the other lower grade traverses, the matrix has lower lithium concentration. The block δ^7Li compositions are positive, while the matrix has a negative δ^7Li composition. The lithium concentration ranges from 8 to 11 ppm in the matrix and 44 to 72 ppm in the block. The δ^7Li ranges from -1.1 to 0‰ in the matrix and from +1.4 to +5.3‰ in the block.

A10-3 Traverse

The measured A10-3 traverse whole-rock Li concentration and isotopic compositions can be seen in Table 9 and Figures 21 and 22.

Table 9: Amphibolite traverse A10-3 Li concentration and δ^7Li composition data.

		Distance from Contact (cm)	*[Li] (ppm)*	*δ^7Li (‰)*
A10-3	Block	16.5	12	-3.1
		15.5	11	-1.7
		13.5	12	-3.5
	Replicate	13.5	11	-1.3
		12.5	13	-4.2
		11.5	11	-2.2
		10.5	10	-2.5

		9.5	8	-3.8
		8.5	11	-1.2
	Replicate	8.5	10	-2.8
		7.5	11	-2.4
		6.5	12	-1.7
	Replicate	6.5	10	-2.3
		5.5	11	-1.6
		4.5	12	-0.8
		3.5	11	0.1
	Replicate	3.5	10	-0.2
		2.5	12	0.1
		1.5	14	1.1
		0.5	13	1.4
	Rind	0.5	14	0.3
		1.5	12	-0.9
		2.5	11	0.5
		3.5	16	-0.7
		4.2	17	0.2
		6.2	16	0.6
		7.2	18	1.1
		8.2	14	0.1
		9.2	15	1.5
		10.1	19	1.1
		11.1	21	-1.6
		12.1	49	7.5
		13.1	15	-0.5
		14.1	10	1.7
		15.1	21	3.4
		16.1	18	1.7

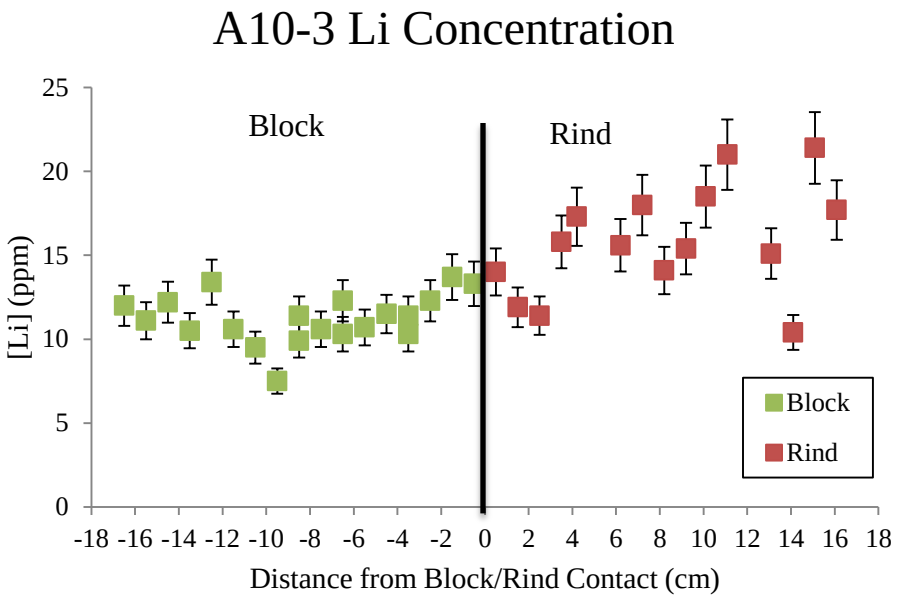

Figure 21: Li concentration for amphibolite traverse A10-3.

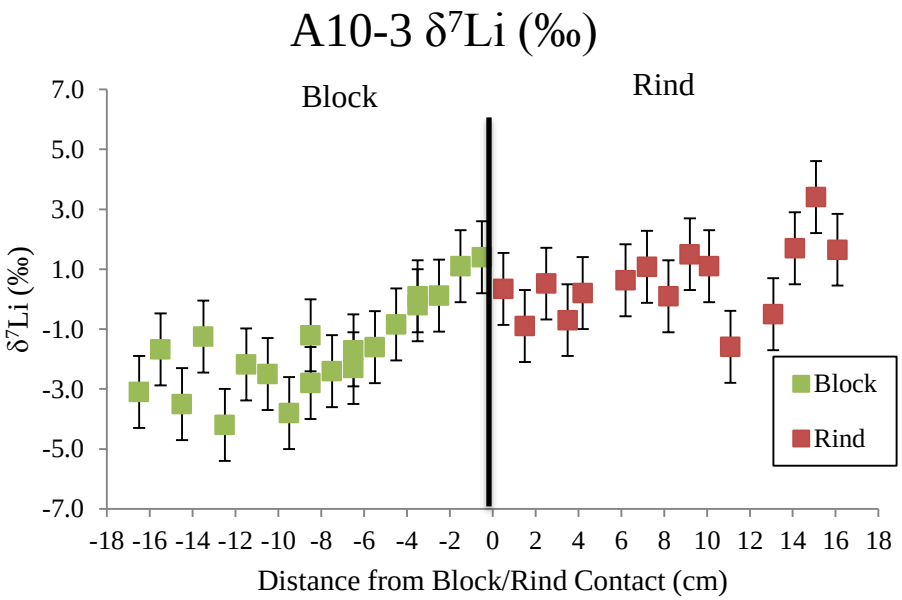

Figure 22: δ^7Li composition for amphibolite traverse A10-3.

The block rind for traverse A10-3 has a higher Li concentration and δ^7Li (16 ppm and 0.6‰) on average when compared to the block core (11 ppm and -1.6‰). There is an increasing trend in the lithium concentrations going across from the block core to the rind. The δ^7Li follows a similar trend. The lithium concentration ranges

from 7.5 to 16 ppm in the block and 10 to 49 ppm in the rind. The δ^7Li ranges from -4.2 to +1.4‰ in the block and -1.6 to +7.5‰ in the rind.

A12-4 Traverse

Table 10 and Figures 23 and 24 display the measured whole-rock lithium concentrations and δ^7Li data for the amphibolite traverse A12-4.

Table 10: Amphibolite traverse A12-4 concentration and δ^7Li composition Li data.

		Distance from Contact (cm)	*[Li] (ppm)*	*δ^7Li (‰)*
A12-4	Block	10.25	15	-4.0
		8.75	14	-4.5
		7.25	14	-5.0
		5.75	14	-6.1
		2.25	16	-0.3
		0.75	17	-1.9
	Rind	0.75	20	-1.2
		2.25	20	-0.1
		3.75	19	-0.1
		5.25	19	-0.9
		6.75	15	0.8
		8.25	19	-0.2
		11	16	1.3

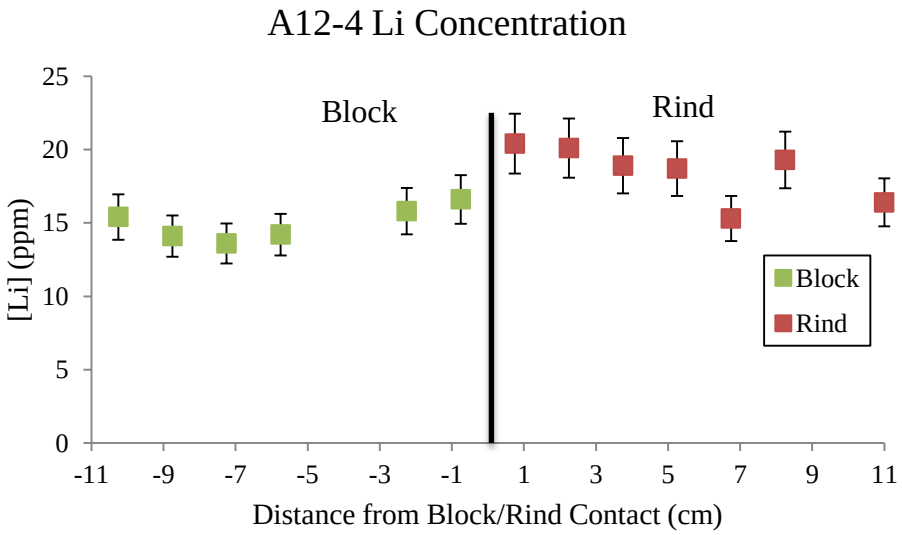

Figure 23: Li concentration in ppm for amphibolite traverse A12-4.

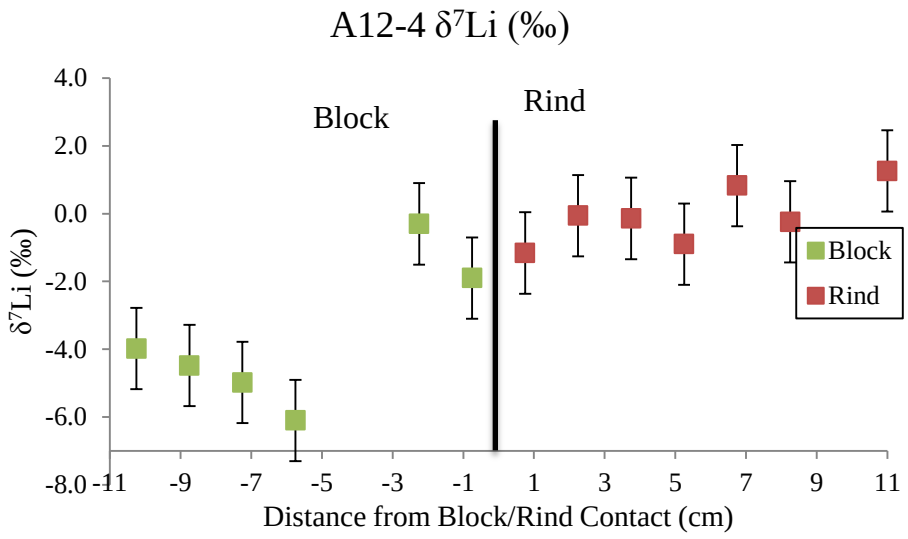

Figure 24: δ^7Li composition for amphibolite traverse A12-4 in per mil.

The block rind for traverse A12-4 has a higher Li concentration and δ^7Li (18 ppm and -0.1‰) on average when compared to the block core (15 ppm and -3.6‰). The A12-4 traverse follows similar trends to the A10-3 traverse, with increasing lithium concentrations and δ^7Li going across the traverse from the block to the rind. The lithium concentration ranges from 14 to 17 ppm in the block core and 15 to 20 ppm in the rind. The δ^7Li values range from -6.1 to -0.3‰ in the block and -1.2 to +1.3‰ in the rind.

Section 5.4: Data Summary

Low-grade

Within the low-grade lawsonite traverse, the blocks have higher concentrations than the matrix. The isotopic data for the matrix is either lower than the block, or overlaps with the block values. In general, there is a very abrupt

transition between the block and matrix with regards to concentration and isotopic composition.

High-grade

In general, the rinds have higher concentrations and isotopic composition than the block cores. However, unlike the lower grade traverses, there is a more gradational change across the core and rind boundary for the concentration and δ^7Li. The Li concentrations and δ^7Li values for these traverses were used to constrain the boundary conditions for simple 1-D numerical models of diffusion and advection (see section 6.3).

Chapter 6: Discussion

The whole-rock Li concentration data collected from the traverses are widely variable within a single lithology within a traverse. This observation is likely due to varying modal proportions of minerals throughout the whole rock. This effect has been seen in previous studies (e.g. Penniston-Dorland et al., 2010). This variation suggests that the variations in whole-rock Li concentrations across traverses may not very useful for differentiating processes such as advection, diffusion and mixing. This variability seen in the whole rock Li concentrations provides justification for focusing on the δ^7Li compositions over the concentration data when comparing data to models.

Measurements of lithium concentrations by LA-ICP-MS in individual amphibole grains were made across the A12-4 traverse. The amphibolite traverse A12-4 was chosen for this purpose because it is large in scale, has large amphibole crystals suitable for Li concentration analysis by LA-ICP-MS, and has a distinct block and rind.

The following figure compares the measured amphibole Li concentrations with the measured whole rock Li concentrations for the A12-4 traverse. The overall trend of increase in Li concentrations from block core to rind in the whole-rock data is reflected in the amphibole data.

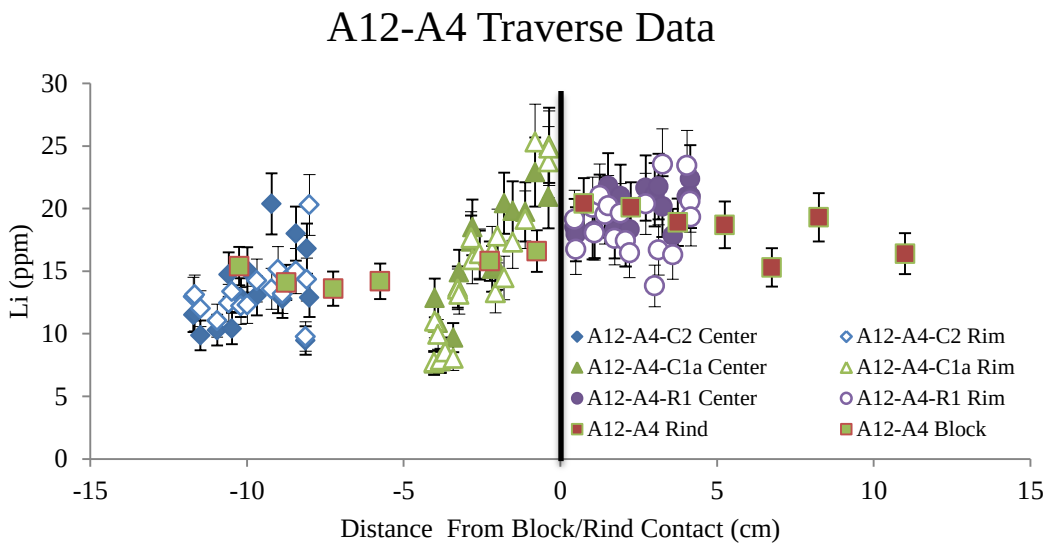

Figure 25: A12-4 laser-ablation data from amphiboles (diamonds, triangles, circles) vs. whole rock block and rind MC-ICP-MS data (squares).

Section 6.1: Mechanisms

The three different mechanisms that may be responsible for variations in lithium isotopic composition and concentration are mechanical mixing, infiltration by advection, and diffusion within an intergranular fluid. These processes represent the major mechanisms of mass transfer in metamorphic systems. Each process leaves a slightly different isotopic and concentration signature, and the use of different models to represent their effect can be helpful in determining which one played the largest role in transporting and depositing lithium in the Catalina Schist mélange zone.

6.1.1 Mechanical Mixing

Mechanical mixing is the physical mixing of different rock types in a mélange zone due to the convergent forces present. Evidence for this mechanism is seen throughout

the Catalina Schist as physical pieces of one rock type being broken off and entrained in another rock type, as seen in Figure 26.

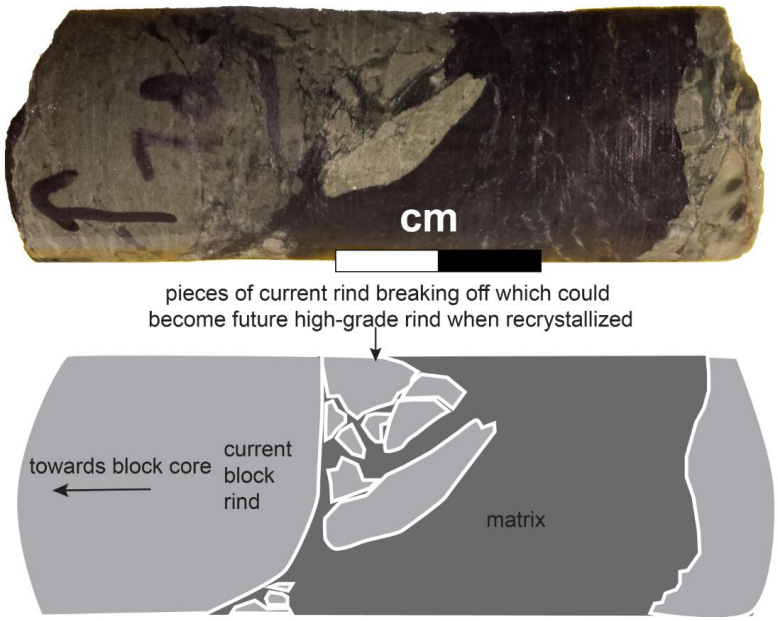

Figure 26: Core from lawsonite-albite facies rocks featuring mechanical mixing. (edited from Penniston-Dorland et al., 2014).

Mechanical mixing has also been documented by variations in highly siderophile element concentrations within the rocks from Catalina Island (Gorman, 2013). If mechanical mixing were a major mechanism controlling lithium concentration, the concentration of the rind would fall between the core and matrix concentrations and there should be widely variable concentrations in the rind. In addition to the intermediate composition and varying concentrations, covariance in lithium concentrations and δ^7Li compositions are expected. These trends are not observed in the δ^7Li data collected from this study. As described above, the whole-rock lithium concentrations are more variable than the isotopic data, which is likely due to small scale modal mineral abundance differences throughout the samples.

6.1.2 Advection

Infiltration of fluids results in transport of Li carried by a metamorphic fluid through a system around grain boundaries. The result of Li transport by advection of a metamorphic fluid could result in a Li concentration in the rind that is different from any of the surrounding rocks. Advection acts as a mechanism to displace the existing gradient between the block and rind, and shift it in the direction of fluid flow. The advection can occur approximately parallel or perpendicular to the block/rind contact. Modeling advection this way has been done previously, for example, in Bickle et al. (1997) and Penniston-Dorland et al. (2008).

6.1.3 Diffusion

Diffusion is the movement of ions due to a chemical potential gradient (or due to thermal gradients). This is usually seen along concentration gradients, moving from higher to lower concentration. This study is concerned with diffusion through an intergranular fluid. Diffusion within an intergranular fluid is likely in these rocks because lithium readily moves into fluids. A characteristic signature for diffusion is that it can leave a smooth transitional gradient between the block and rind for both the lithium concentration and isotopic composition (although in some cases has been observed to create step-like functions across minerals, Richter et al., 2014). This type of smooth profile has been documented previously (Bickle et al., 1997; Teng et al., 2006; Penniston-Dorland et al., 2010). The profiles produced from this study show relatively consistent smooth transitions across the traverses.

Section 6.2: Model Background and Development

Modeling lithium concentration gradients through geologic systems has been done in several studies, notably in rocks adjacent to pegmatites and veins and in blueschist altered from eclogite (John et al., 2012; Liu et al., 2010; Penniston-Dorland et al., 2010; Teng et al., 2006). This modeling has become important for systems with lithium because even across meter-scale distances, lithium can undergo large amounts of diffusive fractionation (Liu et al., 2010), and modeling this diffusion can explain patterns of lithium enrichment in rocks and isotopic variations, including low δ^7Li in rocks. This is due to faster diffusion of ^{6}Li relative to ^{7}Li. Diffusion modeling is also helpful in order to constrain time scales for how long a system has been enriched in isotopically different fluids and allowing diffusion of lithium to occur through the system (Penniston-Dorland et al., 2010; John et al., 2012).

6.2.1 Model Development

Diffusion is described by Fick's second law:

Eqn 6.1 $$\boldsymbol{J = -D\frac{\partial C}{\partial x}}$$

where *J* is the diffusive mass flux, *D* is the diffusion coefficient with units [length^2/time], *C* is the concentration with units [mass/volume], and *x* is the distance across the profile. The *(∂C/∂x)* term gives a concentration gradient along which the ions travel. This equation dictates the distance over which diffusion will occur and the concentrations that result due to the chemical gradient present in the system.

To demonstrate the effect that diffusion has on the lithium isotopic composition and concentration, the measured values are plotted against an ideal diffusion model. The model used, taken from Crank (1975), is:

Eqn 6.2 $$C(x,t) = C_0 - \left(\frac{\Delta C}{2}\right) erfc\left(\frac{x}{2\sqrt{D_e t K_e^{-1}}}\right)$$

where C_0 is the initial concentration of lithium, ΔC is the change in lithium concentration over distance, x is the distance in cm, D_e is the diffusivity in cm^2/s, t is time in years, and K_e is the effective partition coefficient between rock and fluid. This model is one-dimensional and describes diffusion across a planar surface. The model calculates C(x,t) for both ^{6}Li and ^{7}Li. The diffusion coefficients for each isotope are related by the beta factor through the equation:

Eqn 6.3 $$D_6/D_7 = (m_7/m_6)^{\beta}$$

The beta factor, β, is an empirical parameter determined from experimental data (Richter et al., 2003) and m_6 and m_7 are the atomic masses of ^{7}Li and ^{6}Li. The smaller β is, the weaker the isotopic fractionation between the two isotopes (Teng et al., 2006). This β factor has been determined to be between 0.015 for lithium in water at 75°C (Richter et al., 2006) to as high as 0.215 for lithium in silicate melts at 1400°C and 0.27 in pyroxenes (Richter et al., 2014). β values were inferred to range from 0.02 to 0.2 in the Liu et al. (2010) study and 0.12 in Teng et al. (2006) and Penniston-Dorland et al. (2010).

Advection must be integrated into the model separately. Advection can be accounted for through the equation:

Eqn 6.4 $$\frac{\partial C}{\partial t} = \frac{D\partial^2 C}{\partial x^2} + v\frac{\partial C}{\partial x}$$

This equation, from Bear (1972), describes the concentration of a chemical tracer or isotope ratio, C, where D is the bulk diffusion coefficient, t is time, v is the average fluid velocity, and x is distance.

6.2.2 Modeling Examples

The following figure displays an example of a lithium diffusion model for both lithium concentration and δ^7Li composition. The boundary conditions for the concentration were chosen based on the A10-3 traverse, using the average of the four end data points on each end of the rind and core, 8.5 ppm for the core and 13 ppm for the rind. The same was done for the δ^7Li composition, with -2‰ for the core and +1‰ for the rind. The β factor used in this scenario is 0.2. The solution to the diffusion equation (eq. 6.2) results in values of $(Dt/K)^{1/2}$ that represent a diffusive distance. The $(D_7t/K)^{1/2}$ was calculated to be 1.73 and the $(D_6t/K)^{1/2}$ was calculated to be 1.76. The model chosen was based on statistical data taken from the A10-3 traverse and to show the ability to produce a working model.

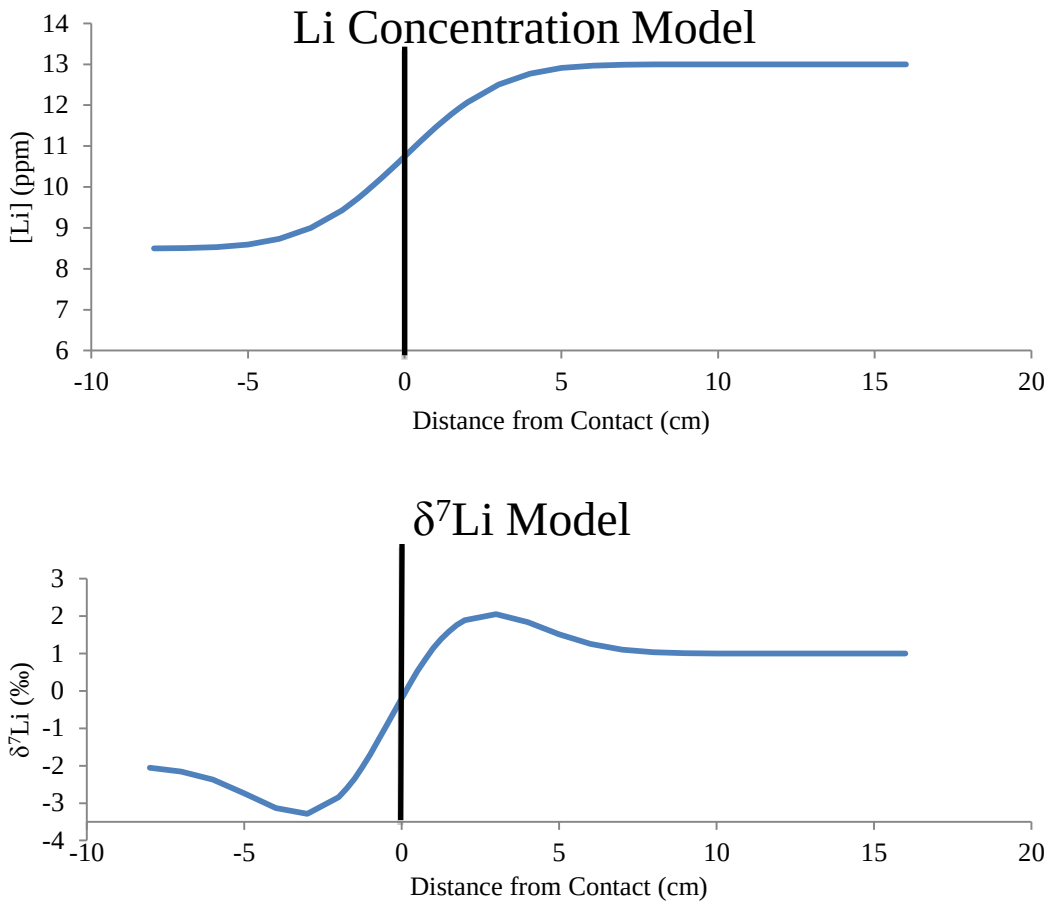

Figure 27: Example lithium concentration and δ^7Li composition model with boundary conditions based on A10-3 traverse data.

6.2.3 Chi-Squared Tests

The chi-squared statistical test was used to find the model solution that best fit the data. The Chi-squared statistical test, in this case, is a measure of how closely the models match the measured values of the lithium concentrations and δ^7Li compositions. This is done following the equation:

Eqn 6.5 $$\boldsymbol{X^2 = \sum \frac{(o-e)^2}{e}}$$

where for each data point the modeled value, *e*, is subtracted from the observed measured value, *o*. The resulting number is squared and divided by the model value.

The results are summed over the entire traverse. The closer the chi-squared value is to 0, the closer the measured values are to the model values. When fitting the data with the model solution, the goal was to minimize the chi-squared value. This was done by an iterative process by first choosing model input values, then calculating a chi-squared value, then modifying the model input values and recalculating chi-squared until a minimum value is reached.

Section 6.3: Models

When the models were produced and compared to the lithium concentration data, the concentration data tended to not be modeled very well. This is likely because the whole-rock lithium concentration is variable in samples across a traverse due to varying mineral modal percentages, as discussed previously. Therefore, during further model development, the δ^7Li composition data were used to produce the most accurate models. This is because δ^7Li is less likely to be affected by concentration differences and mineral modal abundances.

The initial boundary conditions on each side of the model for the concentration and isotopic composition were generally determined by taking the average of the measured values from each side of the traverse far from the contact (where values varied at the contact). For example, when creating the LB13-2 model, the average for all of the matrix concentration values was used to determine a starting concentration on the matrix end, and the average for all of the block concentration values was used to constrain a value for the block end since the change in concentration and isotopic composition was abrupt at the contact. As with other input

factors, the boundary conditions were chosen in order to minimize the model chi-squared value. Table 14 compares the model values with observations.

6.3.1 Lawsonite-Blueschist Facies

The following figures show the model applied to the lawsonite-blueschist facies data from the LB13-2 traverse before and after advection was integrated.

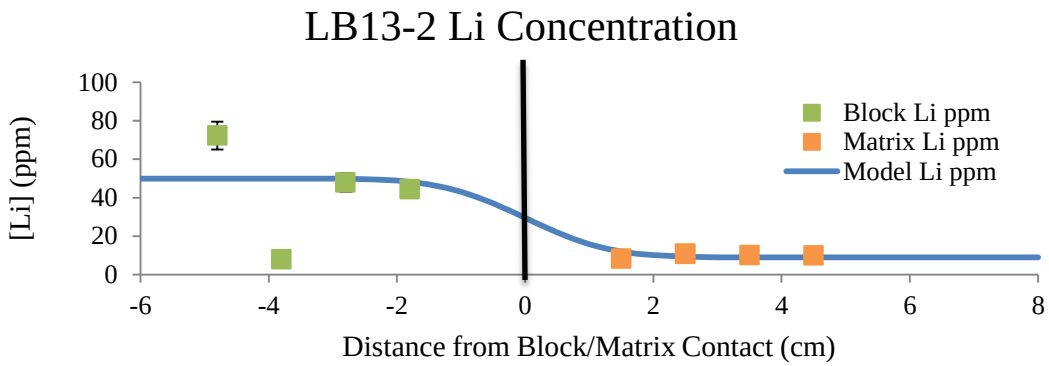

Figure 28a: LB13-2 lithium concentration data with model, where the initial concentration for the block was set to 50 ppm and the initial concentration of the matrix was set to 9 ppm with no advection.

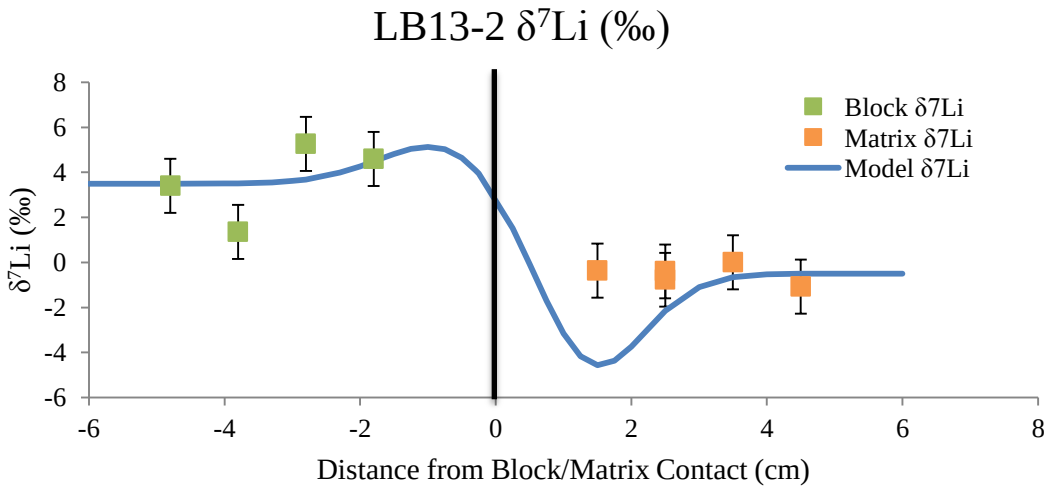

Figure 28b: LB13-2 δ^7Li isotopic data with model, where the initial isotopic value for the block was set to 3.5‰ and the initial isotopic value for the matrix was set to -0.5‰ with no advection.

The boundary conditions for both δ^7Li and lithium concentration were chosen based on the average of the values from the block and for the matrix, then were altered slightly to best minimize the chi-squared value. The lithium concentration model matches the concentration fairly well in the matrix and somewhat in the block, but the isotopic model does not match the isotopic data very well, especially with regards to the matrix. The model underestimates three of the matrix values, as well as one block value, and over-estimates one block value.

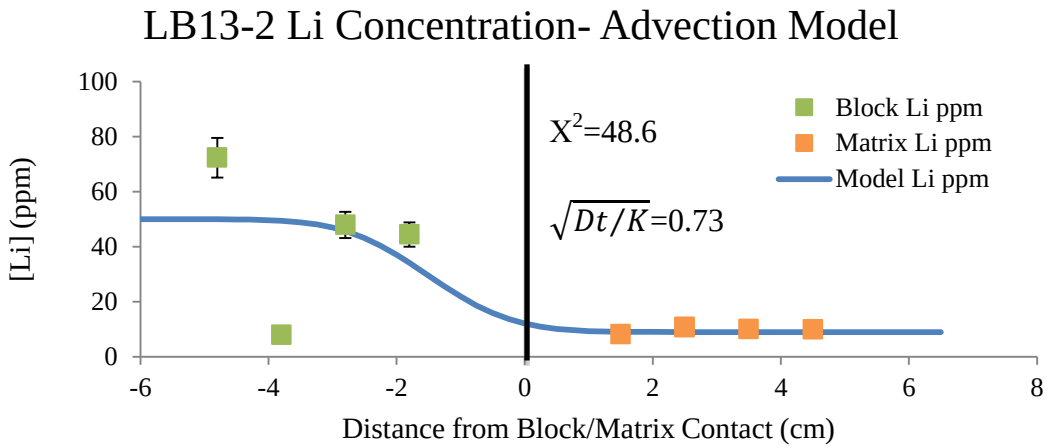

Figure 29a: LB13-2 [Li] data with model results including advection with x* = 1.5 cm.[3]

[3] The value for each traverse is the same for both concentration and isotopic composition and therefore only reported once per set of traverse data.

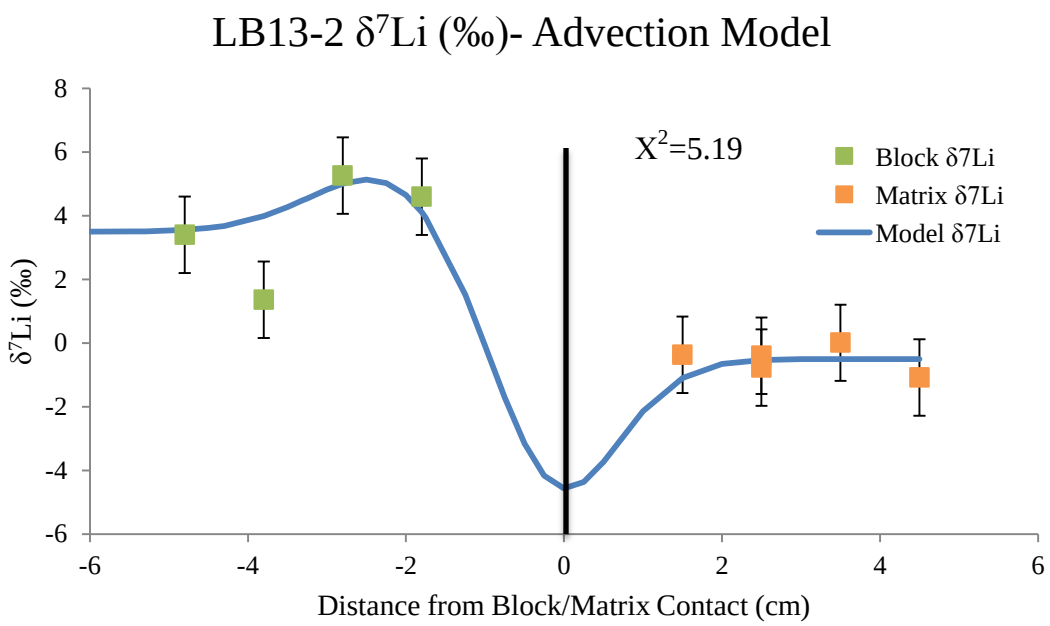

Figure 29b: LB13-2 δ^7Li data with model results including advection with x* = 1.5 cm.

In the above models a solution to the advection-diffusion equation with an advective distance (x*) of 1.5cm was modeled, with the advection moving towards the block. All but one δ^7Li data point fall within uncertainty of the model values. All but two Li concentration data points fall within uncertainty of the model values.

6.3.2 Lawsonite-Albite Facies

The following figures show the best fit models for the lawsonite-albite facies LA13-2 and LA13-3 traverses without accounting for advection. These are followed by the data for the LA traverses with advection. In each case the Li concentration and

δ^7Li are part of the same model.

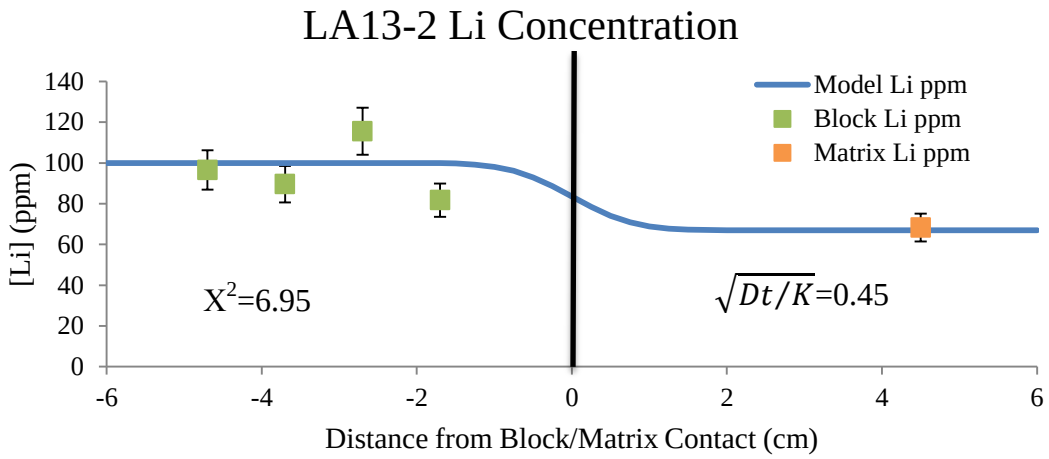

Figure 30a: LA13-2 [Li] with model results. Initial block Li concentration = 100 ppm; initial matrix Li concentration = 67 ppm with no advection.

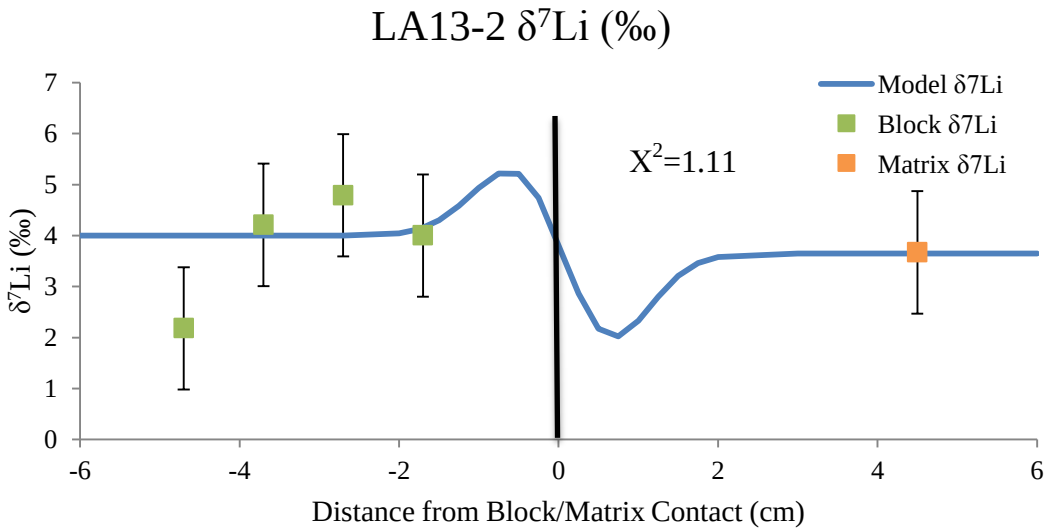

Figure 30b: LA13-2 δ^7Li data with model results. Initial block δ^7Li = 4‰ and initial matrix δ^7Li = 3.65‰ with no advection.

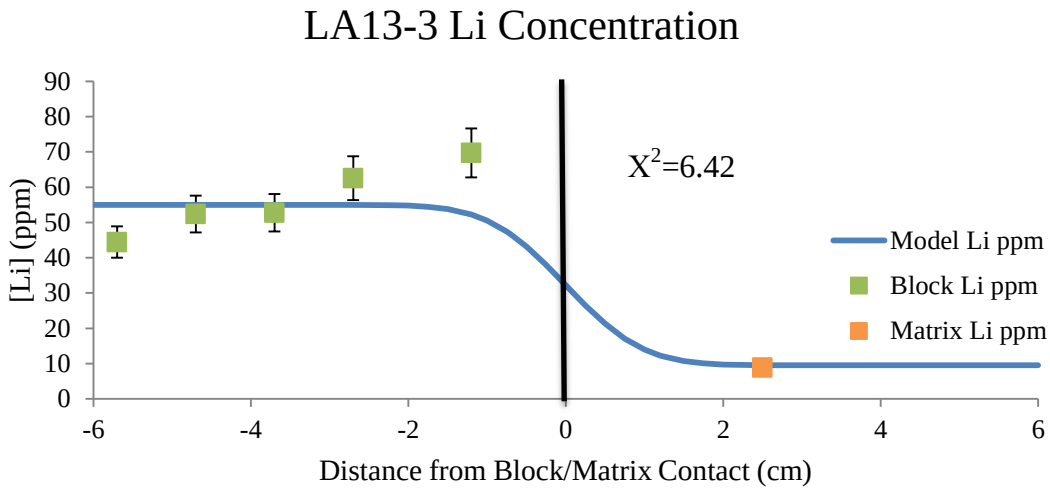

Figure 31a: LA13-3 lithium concentration data with model results. Initial matrix Li concentration = 9.5 ppm and the initial block concentration = 55 ppm with no advection.

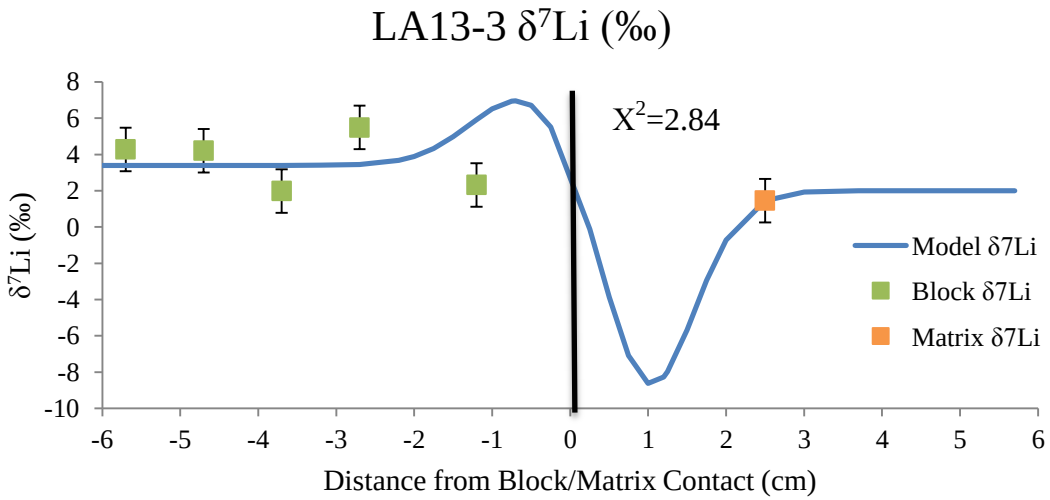

Figure 31b: LA13-3 δ^7Li isotopic data with model results. Initial block δ^7Li = 3.4‰ and the initial matrix δ^7Li = 2‰ with no advection.

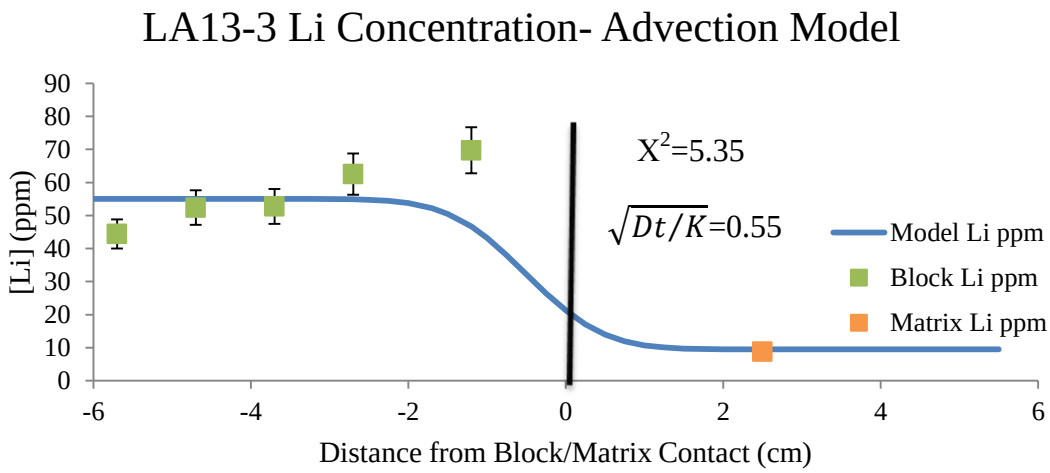

Figure 32a: LA13-3 [Li] data with model results including advection with x* = 0.5 cm.

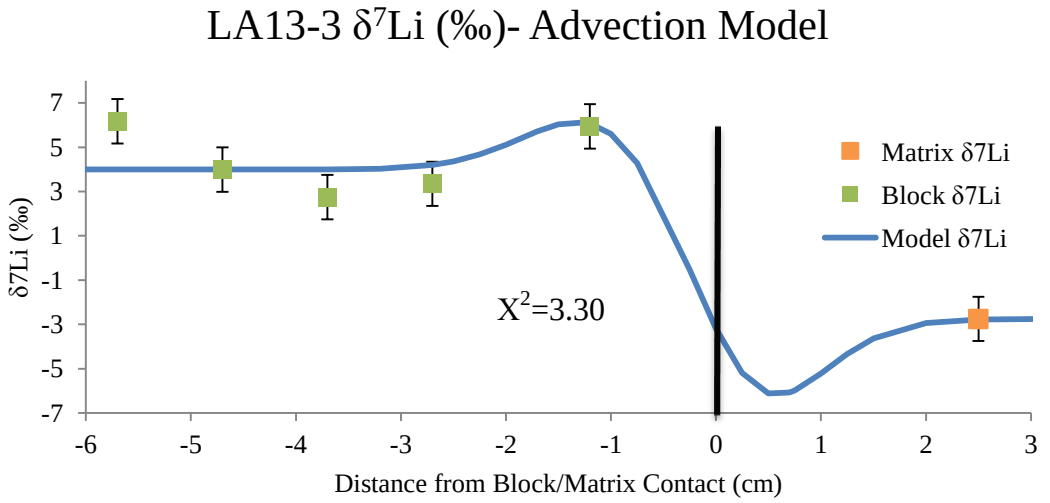

Figure 32b: LA13-3 δ^7Li data with model results including advection with x* = 0.5 cm.

The LA13-2 traverse shows good model fit based on the low χ^2 value, so an advection model was not applied to this set of data. An advection-diffusion model was used for the LA13-3 traverse, with an advective distance (x*) into the block of 0.5 cm to allow for a better model fit to the isotopic data.

6.3.3 Amphibolite Facies

The following figures illustrate the model fit for the two amphibolite facies traverses, A10-3 and A12-4 with and without advection.

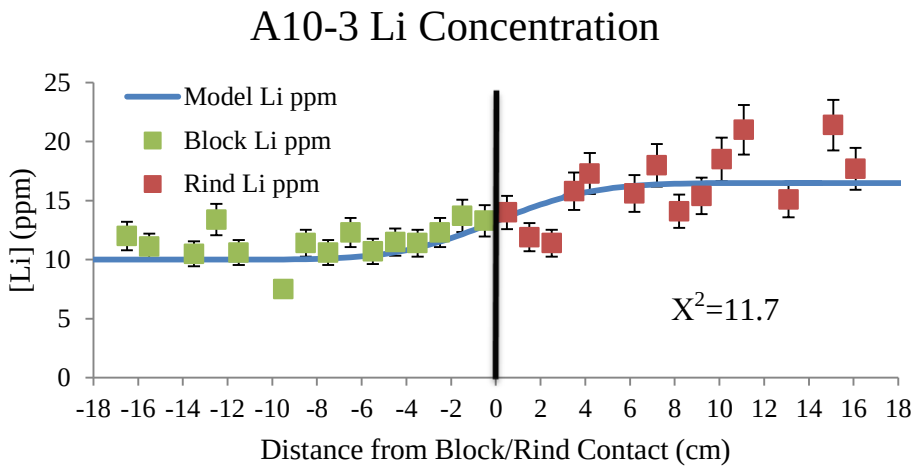

Figure 33a: A10-3 lithium concentration with model, with 10 ppm as the starting concentration for the block and 16.5 ppm as the initial concentration for the rind without advection.

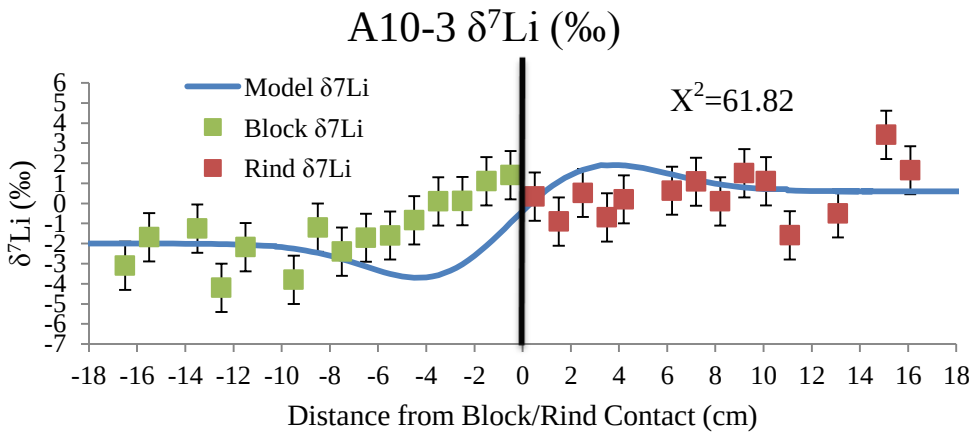

Figure 33b: A10-3 δ^7Li isotopic data with model, with -2.0‰ as the initial composition of the block and 0.6‰ as the initial composition of the rind without advection.

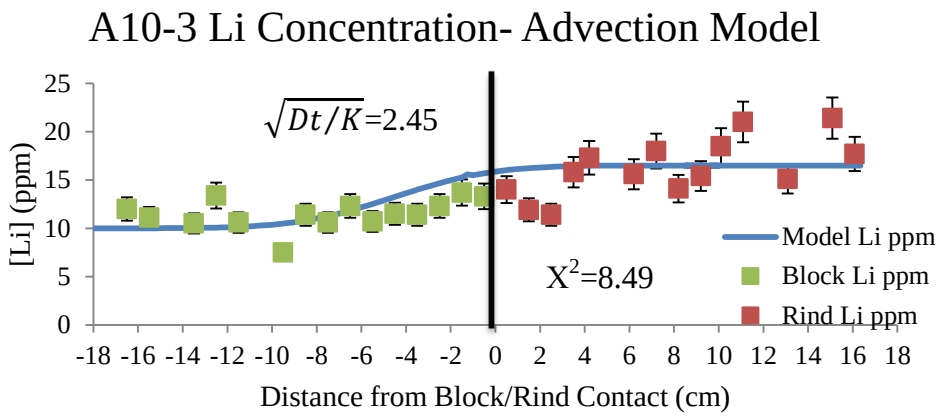

Figure 34a: A10-3 [Li] data with model results including advection with x* = 4.5 cm.

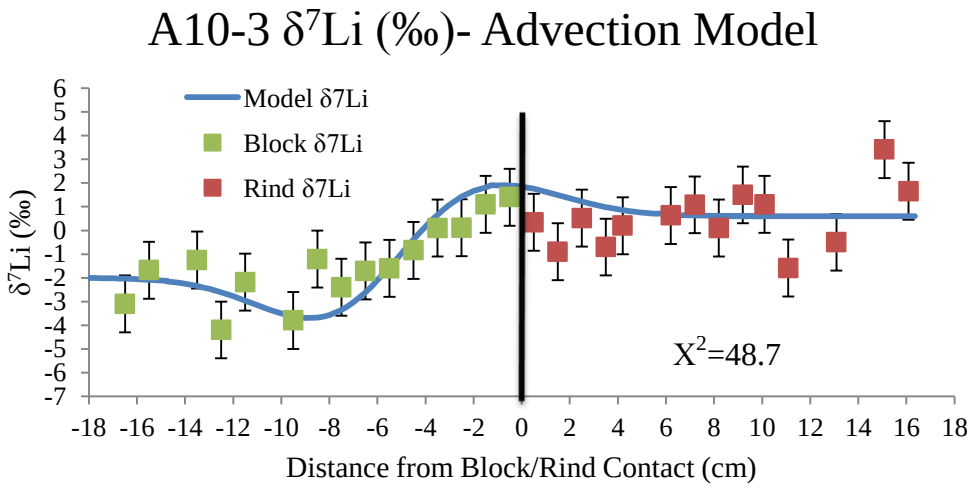

Figure 34b: A10-3 δ^7Li data with model results including advection with x* = 4.5 cm.

Before advection was applied, the A10-3 traverse data for concentration fit the model reasonably well, but the δ^7Li data was very clearly offset from the model in the block. With an advective distance (x*) = 4.5 into the block, the isotopic data fit the model much better as reflected in the lower X^2 values for both concentration and isotopic data.

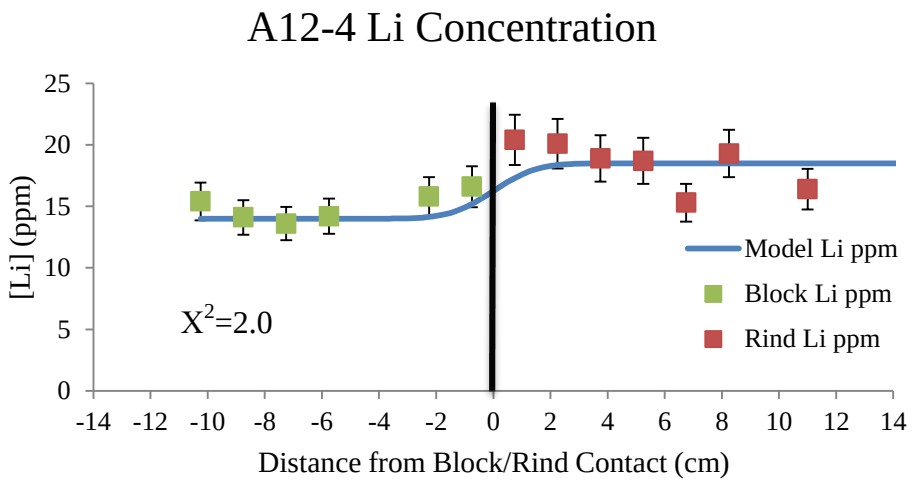

Figure 35a: A12-4 lithium concentration with model, with initial block concentration at 14 ppm and initial rind concentration at 18.5 ppm and no advection.

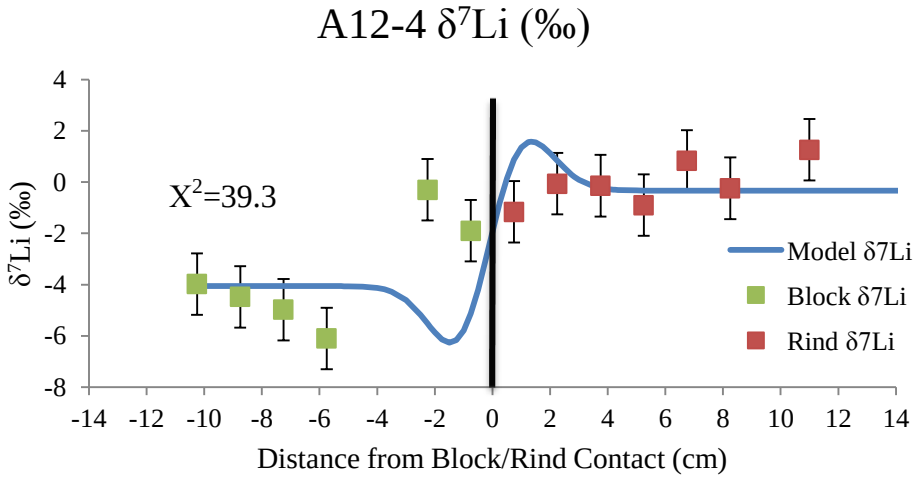

Figure 35b: A12-4 δ^7Li isotopic composition with model, with initial block isotopic composition at -4.1‰ and initial rind composition at -0.33‰ and no advection.

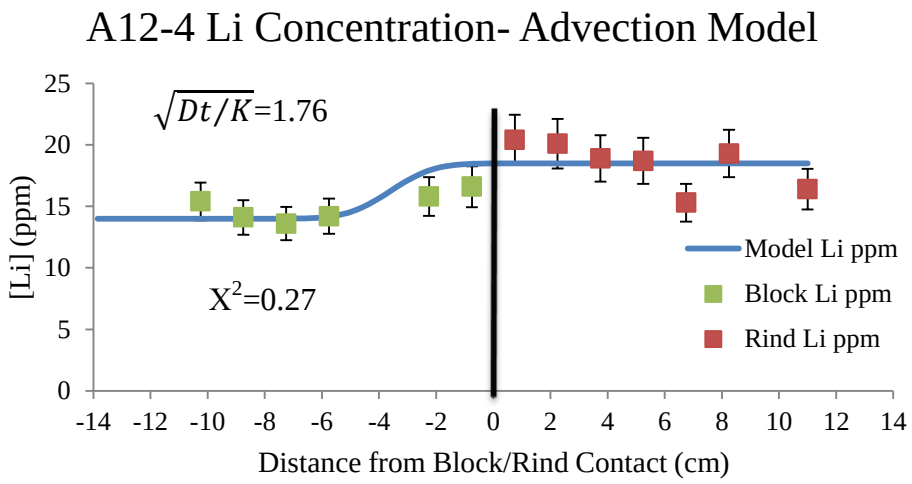

Figure 36a: A12-4 [Li] data with model results including advection with x* = 3.6 cm.

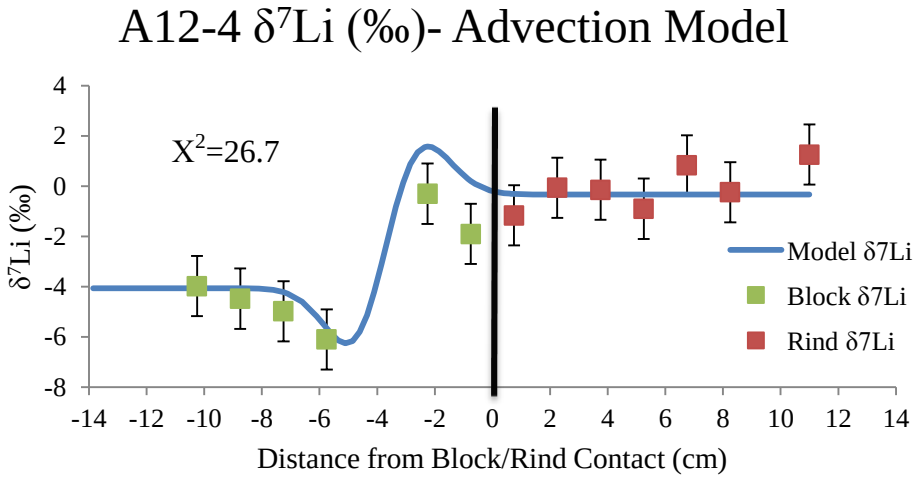

Figure 36b: A12-4 δ^7Li data with model results including advection with x* = 3.6 cm.

The A10-3 traverse had a shift of 4.75 cm applied to the model and the A12-4 traverse had a shift of 3.6 cm applied. The model for the A12-4 traverse concentration fit the data reasonably well, but there was a discrepancy around the boundary between the block and rind, while in the isotopic data traverse, the data peak and trough were

shifted from the model. With an advective distance (x*) of 3.6 into the block the X^2 value was lower for both models and improved the fit to the data.

Section 6.4: Implications

6.4.1 Lithium Source and Composition

The difference in Li concentrations in the mafic rocks of the Catalina Schist compared to their likely protolith (MORB or altered MORB) has been attributed to transport of Li from sedimentary rocks entrained in the mixing zone between the mantle wedge and subducting slab (Penniston-Dorland et al., 2012a). Previous research has found isotopically light lithium compositions in ocean sediments (Bouman et al., 2004), and there is clear evidence of sediments in this complex based on the mélange matrix mineralogical composition and metamafic block compositions (Penniston-Dorland et al., 2012a).

The following plots show the amphibolite grade traverse δ^7Li data and Li concentrations measured from this study along with data for the mélange matrix in the same grade of material from the Catalina Schist.

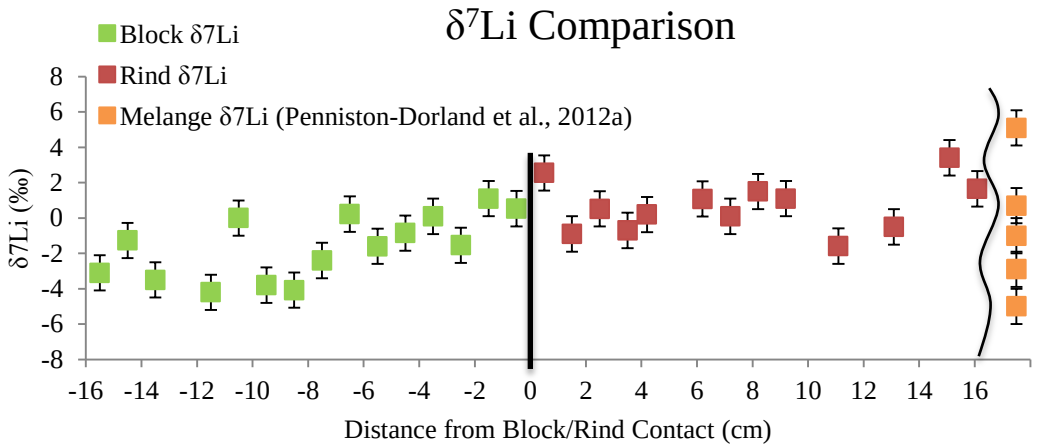

Figure 37a: A10-3 traverse Li isotopic data with Li isotopic and concentration data from Penniston-Dorland et al., 2012a from amphibolite grade mélange matrix. The line represents a break in the distance between the samples analyze

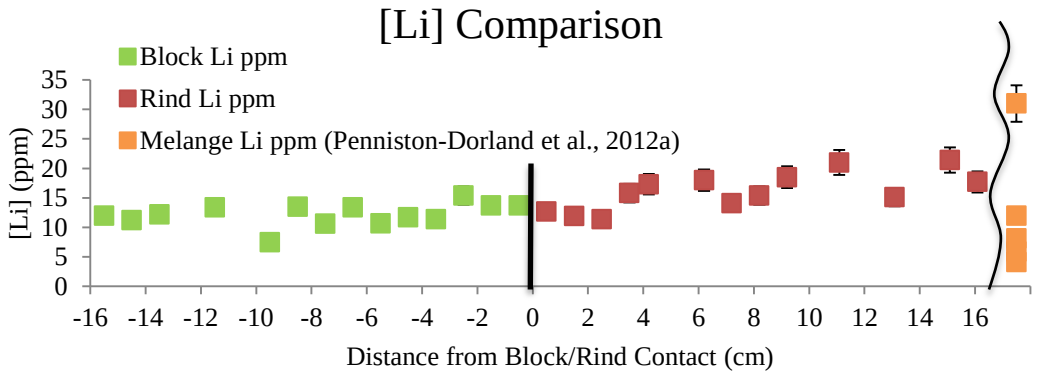

Figure 37b: A10-3 traverse Li concentration data with Li isotopic and concentration data from Penniston-Dorland et al., 2012a from amphibolite grade mélange matrix. The line represents a break in the distance between the samples analyzed between the two studies.

These plots demonstrate that the mélange matrix has heterogeneous isotopic compositions and lithium concentrations. Another interesting note is that in the lower

grades, the mélange matrix has lighter isotopic composition than the blocks, while the higher grade amphibolites show an opposite trend.

6.4.2 Interpretations

In the high grade samples, the rind is enriched in heavier ^{7}Li while the blocks are enriched in the lighter ^{6}Li. The models suggest that the isotopic composition data along the traverses are affected by diffusion and advection because of their shape and how the compositions change across the block/rind and block/matrix boundaries. The models for most of the traverses had to incorporate the affects of advection in order for the model to fit well. Unlike the expected results for mechanical mixing, the data display a gradual change along the traverses. Therefore, it is likely that the Li is being transported in fluids by advection accompanied by diffusion over distances that are small at low metamorphic grades (variations due to diffusion ranging over distances up to ~ 3 cm) to larger distances at higher metamorphic grades (variations due to diffusion ranging over distances up to ~ 15 cm).

6.4.3 Light Lithium Isotopic Composition

One of the major issues to be addressed with this research was to discuss how the blocks achieved such light lithium isotopic compositions (negative $\delta^{7}Li$ ranging down to -6.1‰). Values this low have not been reported for MORB or altered MORB. So far, there is no simple explanation for this light lithium isotopic composition found in these mélange blocks. The amphibolite blocks have the lighter isotopic composition while the lower grade lawsonite-albite and lawsonite-blueschist samples have much heavier isotopic compositions. Diffusive fractionation can account for some of this, which is seen as the slight downward bump that is present in

the isotopic composition models due to the higher diffusivity of ^{6}Li relative to ^{7}Li, but it cannot account for how light the values are in this study. It is not possible to achieve the observed low δ^{7}Li values for the A10-3 block core values starting with typical MORB isotopic compositions. This result suggests that some process occurred during prograde metamorphism that causes the isotopic compositions to shift. One possibility is that prograde dehydration reactions release heavy Li preferentially into fluids (e.g. Zack et al., 2003). While models using available Li partitioning and fractionation factors suggest that this is unlikely (Marschall et al., 2007), the models rely heavily on sparse experimental data (Brenan et al., 1998; Wunder et al., 2006; 2007), The results of this work suggest that more experimental work investigating the partitioning and fractionation of Li among metamorphic minerals are needed.

Appendix

Table 11: Kakanui hornblende EPMA analyses

Analysis	*Na_2O*	*MnO*	*Al_2O_3*	*CaO*	*SiO_2*	*MgO*	*FeO*	*K_2O*	*TiO_2*	*Total*
1	2.65	0.08	15.03	10.33	40.43	12.81	10.97	2.01	4.36	98.7
2	2.72	0.09	14.81	10.16	40.68	12.86	10.78	1.92	4.39	98.4
147	2.62	0.10	14.63	10.24	40.09	12.98	10.97	2.03	4.35	98.0
148	2.63	0.09	14.66	10.35	40.26	12.93	10.81	2.04	4.35	98.1
149	2.62	0.09	14.58	10.30	39.40	12.73	10.45	2.05	4.31	96.5
150	2.69	0.11	14.65	10.32	39.98	12.85	10.77	1.95	4.29	97.6
151	2.66	0.07	14.62	10.35	39.84	12.58	10.88	2.06	4.22	97.3
Average	2.66	0.09	14.71	10.29	40.10	12.82	10.81	2.01	4.33	
Accepted	2.6	0.09	14.9	10.3	40.37	12.8	10.92	2.05	4.72	

Table 12: Major element compositions of amphiboles from A12-A4 measured using EPMA.

Sample Name	*Na_2O*	*FeO*	*CaO*	*Al_2O_3*	*MgO*	*MnO*	*K_2O*	*SiO_2*	*TiO_2*	*Total*
A12-A4-C1a-grain1-C	2.04	14.00	11.00	15.57	11.38	0.07	0.28	44.23	0.91	99.47
A12-A4-C1a-grain1-R	1.97	14.05	10.89	15.29	11.40	0.11	0.29	44.28	0.82	99.09
A12-A4-C1a-grain4-C	1.91	14.55	10.79	15.65	11.01	0.12	0.29	43.87	0.83	99.02
A12-A4-C1a-grain4-R	2.05	13.92	10.73	15.31	11.15	0.08	0.27	44.03	0.85	98.39
A12-A4-C1a-grain5-C	1.98	14.89	10.85	15.39	11.00	0.08	0.29	44.01	0.86	99.35
A12-A4-C1a-grain5-R	1.96	14.46	10.83	15.61	10.78	0.06	0.30	43.69	0.88	98.57
A12-A4-C1a-grain2-C	2.01	14.49	10.85	15.86	10.86	0.05	0.32	43.72	0.89	99.05
A12-A4-C1a-grain2-R	1.92	14.41	10.87	15.76	10.86	0.08	0.30	44.15	0.89	99.25
A12-A4-C1a-grain3-C	2.05	14.58	10.98	16.21	10.71	0.06	0.31	43.04	0.83	98.76
A12-A4-C1a-grain3-R	2.05	14.64	10.83	16.38	10.62	0.06	0.29	43.58	0.87	99.32
A12-A4-C1a-grain6-C	1.79	13.91	10.81	13.90	11.98	0.09	0.23	44.82	0.85	98.38
A12-A4-C1a-grain6-R	1.75	13.84	10.84	13.63	12.30	0.09	0.25	45.27	0.80	98.77
A12-A4-C1a-grain7-C	2.01	13.94	10.97	14.76	11.32	0.09	0.26	43.72	0.85	97.91
A12-A4-C1a-grain7-R	2.09	14.09	10.89	14.97	11.19	0.09	0.26	44.06	0.74	98.39
A12-A4-C1a-grain8-C	1.87	13.13	10.27	14.64	11.51	0.07	0.25	43.51	0.82	96.07
A12-A4-C1a-grain8-R	1.95	13.97	10.83	14.16	11.89	0.04	0.24	44.47	0.86	98.42
A12-A4-C1a-grain9-C	1.86	13.56	10.85	14.18	11.78	0.09	0.24	44.84	0.82	98.21
A12-A4-C1a-grain9-R	1.91	13.39	11.04	14.17	11.98	0.08	0.25	44.33	0.87	98.01
A12-A4-C1a-grain11-C	1.99	13.36	10.91	14.81	11.95	0.06	0.26	44.57	0.82	98.73
A12-A4-C1a-grain11-R	2.13	12.97	10.99	15.08	11.80	0.04	0.26	44.17	0.83	98.27
A12-A4-C1a-grain10-C	2.03	13.84	10.93	14.92	11.41	0.07	0.26	44.01	0.82	98.30
A12-A4-C1a-grain10-R	1.95	13.87	10.87	14.86	11.50	0.08	0.27	43.93	0.84	98.17
A12-A4-C1a-grain14-C	1.85	13.34	10.39	14.48	12.45	0.05	0.26	44.89	0.81	98.51
A12-A4-C1a-grain14-R	2.01	12.79	10.96	13.51	12.61	0.04	0.23	45.24	0.67	98.05
A12-A4-C1a-grain12-C	1.80	13.61	10.90	13.90	12.30	0.06	0.23	44.98	0.79	98.56

A12-A4-C1a-grain12-R	1.70	12.36	11.10	12.81	13.37	0.06	0.16	46.28	0.42	98.28
A12-A4-C1a-grain13-C	1.71	13.36	10.77	13.50	12.64	0.07	0.22	45.20	0.80	98.27
A12-A4-C1a-grain13-R	1.81	12.84	10.94	13.66	12.90	0.05	0.21	45.27	0.69	98.36
A12-A4-C1a-grain15-C	1.89	13.63	10.66	15.65	11.50	0.06	0.31	43.75	0.90	98.34
A12-A4-C1a-grain15-R	1.92	13.12	10.86	14.93	11.96	0.10	0.27	44.10	0.84	98.09
A12-A4-C1a-grain16-C	2.00	13.12	10.67	14.62	12.40	0.07	0.26	44.51	0.76	98.42
A12-A4-C1a-grain16-R	1.90	12.67	10.46	14.06	12.48	0.07	0.26	44.55	0.80	97.25
A12-A4-C1a-grain17-C	1.87	13.73	10.55	14.58	11.89	0.10	0.23	44.35	0.76	98.05
A12-A4-C1a-grain17-R	1.91	13.64	10.42	14.39	12.05	0.09	0.23	44.87	0.68	98.27
A12-A4-C1a-grain18-C	1.98	14.37	10.24	15.28	11.60	0.14	0.25	43.87	0.87	98.60
A12-A4-C1a-grain18-R	2.15	14.11	10.41	15.05	11.68	0.15	0.26	43.97	0.73	98.50
A12-A4-C1a-grain20-C	2.07	13.68	10.07	14.96	12.04	0.17	0.24	44.25	0.86	98.33
A12-A4-C1a-grain20-R	2.14	13.44	10.02	15.45	12.05	0.16	0.23	43.76	0.74	97.98
A12-A4-C1a-grain19-C	2.10	14.28	10.13	15.16	11.72	0.16	0.24	44.04	0.84	98.68
A12-A4-C1a-grain19-R	2.04	14.11	10.09	15.59	11.48	0.15	0.24	43.77	0.85	98.33
A12-A4-C2a-grain1-C	1.83	12.28	10.49	14.80	12.84	0.16	0.24	44.95	0.79	98.37
A12-A4-C2a-grain1-R	1.86	12.21	10.77	14.83	12.97	0.14	0.21	44.96	0.70	98.64
A12-A4-C2a-grain2-C	1.85	12.13	10.37	14.69	12.92	0.12	0.24	44.82	0.66	97.80
A12-A4-C2a-grain2-R	1.88	12.01	10.64	14.74	13.00	0.14	0.21	44.66	0.81	98.09
A12-A4-C2a-grain3-C	1.96	12.45	10.39	14.70	12.90	0.14	0.21	44.79	0.73	98.26
A12-A4-C2a-grain3-R	2.06	12.16	10.75	14.46	12.74	0.13	0.23	44.71	0.72	97.95
A12-A4-C2a-grain7-C	1.94	11.90	10.61	14.50	12.99	0.12	0.24	44.91	0.76	97.97
A12-A4-C2a-grain7-R	1.94	11.97	10.46	14.53	12.87	0.15	0.23	45.10	0.57	97.82
A12-A4-C2a-grain5-C	1.96	12.31	10.53	14.55	12.99	0.17	0.23	44.64	0.82	98.20
A12-A4-C2a-grain5-R	1.92	11.59	10.54	14.47	13.11	0.13	0.23	44.98	0.61	97.58
A12-A4-C2a-grain4-C	1.93	12.03	10.61	14.67	13.18	0.13	0.25	44.86	0.77	98.44
A12-A4-C2a-grain4-R	1.84	12.23	10.44	14.52	12.83	0.12	0.20	44.60	0.84	97.63

A12-A4-C2a-grain6-C	2.04	11.43	10.68	14.60	12.82	0.13	0.26	44.95	0.75	97.65
A12-A4-C2a-grain6-R	2.05	11.43	10.58	14.38	12.92	0.12	0.22	45.05	0.68	97.43
A12-A4-C2a-grain17-C	1.89	12.43	10.68	14.64	12.57	0.08	0.25	45.02	0.73	98.28
A12-A4-C2a-grain17-R	1.87	12.11	10.74	14.17	12.90	0.09	0.21	45.09	0.67	97.85
A12-A4-C2a-grain16-C	1.88	12.43	10.91	14.00	12.44	0.06	0.23	45.20	0.72	97.86
A12-A4-C2a-grain16-R	1.94	12.17	10.77	14.46	12.57	0.09	0.22	45.28	0.72	98.21
A12-A4-C2a-grain15-C	1.88	12.85	11.01	14.22	12.12	0.06	0.26	44.68	0.80	97.86
A12-A4-C2a-grain15-R	1.90	12.88	10.96	14.51	12.32	0.05	0.22	44.40	0.77	98.02
A12-A4-C2a-grain8-C	1.91	13.53	10.97	15.06	11.57	0.05	0.27	43.52	0.86	97.74
A12-A4-C2a-grain8-R	1.99	12.86	11.08	14.05	12.01	0.05	0.25	44.65	0.68	97.63
A12-A4-C2a-grain9-C	1.92	13.20	10.91	15.05	11.41	0.05	0.31	43.61	0.88	97.33
A12-A4-C2a-grain9-R	1.84	12.53	11.06	13.56	12.90	0.02	0.20	45.74	0.46	98.31
A12-A4-C2a-grain10-C	1.84	13.28	10.57	14.38	11.94	0.09	0.26	44.57	0.84	97.77
A12-A4-C2a-grain10-R	1.86	12.83	11.00	14.06	12.50	0.02	0.25	44.86	0.70	98.08
A12-A4-C2a-grain14-C	1.86	12.77	11.09	14.08	12.43	0.07	0.24	45.10	0.73	98.38
A12-A4-C2a-grain14-R	1.88	12.16	9.87	12.63	12.24	0.07	0.18	44.99	0.39	94.41
A12-A4-C2a-grain13-C	1.72	13.23	11.15	13.90	12.10	0.04	0.26	44.59	0.79	97.77
A12-A4-C2a-grain13-R	1.82	12.49	11.15	12.68	13.27	0.05	0.17	46.47	0.47	98.56
A12-A4-C2a-grain12-C	1.88	13.34	10.93	15.25	11.54	0.09	0.30	43.98	0.91	98.21
A12-A4-C2a-grain12-R	1.83	12.94	11.10	13.94	12.43	0.09	0.25	45.06	0.79	98.43
A12-A4-C2a-grain11-C	1.70	13.75	11.06	14.10	12.22	0.05	0.25	44.40	0.80	98.32
A12-A4-C2a-grain11-R	1.85	13.23	10.95	13.70	12.30	0.03	0.24	44.78	0.64	97.73
A12-A4-C2-grain16-C	1.88	11.55	10.33	13.64	13.69	0.10	0.24	46.05	0.68	98.16
A12-A4-C2-grain16-R	1.85	11.10	10.97	13.36	13.74	0.09	0.21	46.85	0.44	98.61
A12-A4-C2-grain10-C	2.15	11.31	10.85	15.00	12.83	0.09	0.23	45.13	0.70	98.28
A12-A4-C2-grain10-R	1.96	11.37	10.80	13.90	13.50	0.15	0.20	46.15	0.63	98.66
A12-A4-C2-grain12-C	2.01	11.41	10.59	14.40	13.46	0.17	0.21	45.82	0.62	98.69

A12-A4-C2-grain12-R	1.97	11.26	10.83	14.11	13.31	0.13	0.21	45.65	0.58	98.05
A12-A4-C2-grain11-C	1.84	11.61	7.93	13.66	13.76	0.17	0.14	46.11	0.59	95.80
A12-A4-C2-grain11-R	1.99	11.78	7.11	14.25	13.49	0.11	0.13	45.97	0.54	95.37
A12-A4-C2-grain4-C	1.91	11.69	10.76	13.99	13.97	0.18	0.18	46.91	0.63	100.22
A12-A4-C2-grain4-R	1.95	11.11	10.53	13.72	13.67	0.15	0.19	46.17	0.67	98.15
A12-A4-C2-grain8-C	2.06	11.72	10.52	14.52	13.20	0.11	0.22	45.67	0.75	98.77
A12-A4-C2-grain8-R	1.90	11.33	10.91	13.94	13.72	0.17	0.21	46.03	0.58	98.78
A12-A4-C2-grain14-C	1.91	11.44	10.46	13.47	13.72	0.15	0.21	46.15	0.71	98.22
A12-A4-C2-grain14-R	1.97	11.22	10.73	13.87	13.76	0.18	0.22	46.04	0.68	98.66
A12-A4-C2-grain6-C	1.96	11.93	10.50	14.16	13.33	0.13	0.23	45.28	0.80	98.32
A12-A4-C2-grain6-R	1.92	11.34	10.65	13.82	13.72	0.16	0.20	45.70	0.72	98.23
A12-A4-C2-grain5-C	1.95	11.87	10.38	13.89	13.61	0.20	0.20	46.15	0.72	98.97
A12-A4-C2-grain5-R	1.95	11.28	10.66	14.15	13.46	0.15	0.20	45.19	0.61	97.65
A12-A4-C2-grain2-C	2.05	11.35	10.67	14.46	13.46	0.15	0.24	45.51	0.78	98.68
A12-A4-C2-grain2-R	1.91	11.65	10.55	13.71	13.76	0.17	0.21	45.76	0.64	98.34
A12-A4-C2-grain3-C	1.91	11.49	10.56	14.00	13.94	0.18	0.21	45.63	0.67	98.58
A12-A4-C2-grain3-R	1.96	11.77	10.62	13.98	13.64	0.16	0.20	45.48	0.73	98.54
A12-A4-C2-grain7-C	2.01	12.20	10.74	14.55	12.52	0.14	0.24	44.49	0.85	97.74
A12-A4-C2-grain7-R	1.95	11.59	10.67	14.49	12.82	0.13	0.21	45.13	0.70	97.70
A12-A4-C2-grain9-C	1.85	11.81	10.45	14.11	13.61	0.12	0.19	45.58	0.66	98.39
A12-A4-C2-grain9-R	1.98	11.72	10.67	14.30	13.58	0.12	0.23	45.43	0.70	98.73
A12-A4-C2-grain13-C	1.92	11.93	10.48	14.05	13.53	0.17	0.24	45.81	0.78	98.89
A12-A4-C2-grain13-R	1.85	11.53	10.99	14.09	13.45	0.12	0.19	45.92	0.53	98.67
A12-A4-C2-grain1-C	1.90	11.97	10.40	13.71	13.61	0.12	0.20	45.57	0.68	98.16
A12-A4-C2-grain1-R	2.00	12.13	10.49	14.31	13.19	0.11	0.23	45.25	0.64	98.36
A12-A4-C2-grain15-C	1.86	12.15	10.65	13.97	13.12	0.14	0.22	45.00	0.68	97.79
A12-A4-C2-grain15-R	1.87	11.69	10.64	13.24	13.33	0.13	0.20	46.18	0.47	97.74

A12-A4-R1-grain2-C	1.81	10.43	10.25	12.82	14.35	0.18	0.16	46.46	0.56	97.02
A12-A4-R1-grain2-R	2.34	10.25	10.19	13.02	14.45	0.20	0.16	46.09	0.51	97.20
A12-A4-R1-grain7-C	1.91	10.47	10.23	13.23	14.67	0.18	0.18	46.09	0.59	97.55
A12-A4-R1-grain7-R	1.91	10.71	9.93	13.47	14.49	0.19	0.18	46.16	0.55	97.59
A12-A4-R1-grain3-C	1.82	10.55	10.15	13.20	14.41	0.16	0.19	46.65	0.56	97.69
A12-A4-R1-grain3-R	1.84	10.33	10.04	13.38	14.54	0.17	0.13	46.90	0.49	97.82
A12-A4-R1-grain1-C	1.74	10.47	10.23	12.54	14.77	0.16	0.15	47.12	0.56	97.74
A12-A4-R1-grain1-R	1.76	10.56	10.22	12.77	15.00	0.17	0.15	46.89	0.55	98.06
A12-A4-R1-grain5-C	1.83	10.29	10.41	12.65	14.90	0.19	0.15	46.75	0.50	97.66
A12-A4-R1-grain5-R	1.83	10.19	10.14	12.67	15.07	0.16	0.13	46.86	0.50	97.54
A12-A4-R1-grain8-C	1.84	9.90	10.12	12.89	14.82	0.16	0.17	46.37	0.67	96.93
A12-A4-R1-grain8-R	1.91	9.67	9.97	12.95	15.05	0.20	0.18	46.36	0.65	96.94
A12-A4-R1-grain9-C	1.95	10.38	10.22	13.01	14.76	0.19	0.16	46.64	0.53	97.85
A12-A4-R1-grain9-R	2.13	10.28	11.03	11.72	14.24	0.15	0.18	47.26	0.38	97.36
A12-A4-R1-grain11-C	1.56	8.54	10.60	11.39	16.52	0.20	0.14	47.80	0.41	97.17
A12-A4-R1-grain11-R	1.55	8.73	10.27	11.72	15.54	0.21	0.12	47.55	0.47	96.16
A12-A4-R1-grain6-C	1.71	10.48	9.99	12.58	15.03	0.18	0.16	47.00	0.61	97.74
A12-A4-R1-grain6-R	1.78	10.12	10.43	12.95	14.91	0.19	0.15	46.80	0.48	97.81
A12-A4-R1-grain10-C	1.69	9.40	10.29	12.22	15.69	0.20	0.16	47.29	0.55	97.50
A12-A4-R1-grain10-R	1.70	9.67	10.36	11.92	15.63	0.17	0.16	47.65	0.49	97.74
A12-A4-R1-grain4-C	1.74	10.43	10.23	12.88	15.06	0.20	0.18	46.50	0.58	97.81
A12-A4-R1-grain4-R	2.08	10.13	10.39	12.99	14.49	0.18	0.15	46.62	0.56	97.60
A12-A4-R1-grain14-C	1.86	10.43	10.19	13.21	14.95	0.20	0.16	46.31	0.55	97.86
A12-A4-R1-grain14-R	1.78	10.25	9.99	13.07	15.02	0.20	0.17	46.42	0.58	97.47
A12-A4-R1-grain15-C	1.83	10.38	10.46	13.62	14.39	0.17	0.22	45.85	0.59	97.52
A12-A4-R1-grain15-R	2.34	10.54	10.43	13.51	14.21	0.18	0.18	45.84	0.58	97.79
A12-A4-R1-grain13-C	2.11	10.35	10.43	14.69	13.67	0.18	0.22	45.29	0.83	97.76

A12-A4-R1-grain13-R	2.05	10.21	10.25	13.27	14.60	0.19	0.15	46.48	0.57	97.77
A12-A4-R1-grain12-C	1.79	10.86	9.95	13.12	14.59	0.17	0.18	46.29	0.68	97.62
A12-A4-R1-grain12-R	1.84	10.64	10.10	13.15	14.74	0.20	0.17	46.65	0.59	98.09
A12-A4-R1-grain19-C	1.74	10.10	10.51	12.60	15.30	0.16	0.15	47.38	0.34	98.27
A12-A4-R1-grain19-R	2.07	9.88	9.57	13.19	14.60	0.21	0.17	46.77	0.63	97.08
A12-A4-R1-grain18-C	1.83	10.36	10.27	12.55	15.21	0.17	0.17	46.78	0.55	97.86
A12-A4-R1-grain18-R	2.22	10.64	10.12	13.26	14.59	0.19	0.16	46.60	0.63	98.39
A12-A4-R1-grain17-C	1.90	10.15	10.66	13.38	14.66	0.16	0.20	46.05	0.69	97.85
A12-A4-R1-grain17-R	1.90	10.51	10.45	13.54	14.66	0.16	0.19	46.24	0.62	98.28
A12-A4-R1-grain16-C	2.00	10.36	10.20	12.88	14.81	0.21	0.16	46.62	0.60	97.85
A12-A4-R1-grain16-R	2.27	10.00	10.62	13.16	14.47	0.16	0.15	46.69	0.47	98.01

Table 13: LA-ICP-MS Standard Data

Standard	*Li (ppm)*	*^{11}B (ppm)*	*SiO_2 (wt%)*	*CaO (wt%)*
NIST 610 Accepted Value	468	350	70	12
NIST 610 Measured	472	354	70	11
	456	340	69	11
	428	321	64	11
	470	350	69	11
	471	348	70	11
	457	346	68	11
	462	345	70	11
	466	349	68	11
	477	358	70	11.4
	450	336	68	11.4
	461	355	69	11.4

	467	338	70	11.4
	462	353	69	11
	466	341	69	11
	497	328	70	11
	431	366	68	11
	493	334	70	11
	435	359	68	11
	463	325	69	11
	465	369	69	11
	483	363	69	11
	445	330	69	11
	467	343	69	11
	461	351	69	11
	499	315	68	11
	428	379	70	11
	453	354	69	11
	476	340	69	11
	467	341	69	11
	461	353	69	11
	465	342	69	11
	463	352	69	11
	462	354	69	11.4
	466	340	70	11.4
	465	353	70	11.4

	463	341	68	11.4
	461	296	69	11.40
	467	400	69	11.40
	443	264	68	11
	487	529	70	11
	460	361	68	11
	468	333	71	11
	466	343	69	11
	461	351	69	11
Average NIST610	463	349	69	11
2σ Standard Deviation	24.1	69.5	2.1	
Percent Relative Error (2σ)	5	20	3	
BCR2g Accepted Value	10	3.0	54	7.0
BCR2g Measured	9.1	4.6	53	7.0
	9.3	7.0	53	7.1
	8.9	6.3	55	7.1
	9.3	7.2	55	7.2
	8.0	4.9	54	7.0
	8.9	4.5	53	7.0
	8.3	5.3	54	7.0
	8.6	3.8	53	7.0
Average BCR2g	7.9	5.5	54.6	7.0
2σ Standard Deviation	0.94	2.47	1.87	
Percent Relative Error (2σ)	27	45	3	

Table 14: Li concentrations of amphiboles measured by LA-ICP-MS.

Traverse	*Type*	*Sample*	*Li (ppm)*	*^{11}B (ppm)*	*SiO_2 (wt%)*	*CaO (wt%)*	*Intensity (%)*	*Energy Density (J/cm^2)*
A12-A4-C2	Core	grain15R	13	6.8	48	10.6	55	3.2
		grain7R	13	6.7	49	10.7	55	3.14
		grain1R	12	6.8	48	10.5	55	3.45
		grain3R	11	5.2	50	10.6	55	3.02
		grain2R	12	5.1	47	10.5	55	2.83
		grain5R	13	3.9	48	10.7	55	2.83
		grain6R	12	7.3	50	10.6	55	2.65
		grain4R	12	6.4	49	11	55	2.59
		grain14R	14	5.3	48	11	55	2.34
		grain8R	14	5.6	47	11	55	1.85
		grain13R	15	3.4	51	11	55	2.06
		grain9R	13	6.2	49	11	55	2.46
		grain12R	15	3.9	50	11	55	2.1
		grain11R	9.8	4.3	34	7.1	59	3.51
		grain10R	14	5.8	50	11	55	1.73
		grain16R	20	8.2	51	11	55	1.79
		grain15C	12	7.5	48	10.7	55	3.45
		grain7C	12	11	48	10.7	55	2.46
		grain1C	9.9	6.6	47	10.4	55	3.45
		grain3C	10	4.7	49	10.6	55	3.08
		grain2C	15	9.4	48	10.7	55	3.08
		grain5C	10	4.9	49	10.4	55	2.73
		grain6C	13	8.3	50	10.5	55	2.77
		grain4C	15	7.3	49	11	55	2.4
		grain14C	13	5.8	48	10	55	2.46
		grain8C	20	7.0	52	11	55	1.66
		grain13C	13	5.3	47	10	55	1.91
		grain9C	13	4.6	48	10	55	2.28
		grain12C	18	3.3	50	11	55	1.66

	grain11C	9.5	5.5	38	7.9	59	3.33
	grain10C	17	10	49	11	59	3.33
	grain16C	13	4.2	48	10	55	1.91
A12-A4-C1a	grain2R	7.7	<2.06	49	11	57	2.34
	grain1R	11	<2.23	47	11	57	2.65
	grain4R	9.9	<2.21	46	11	57	2.65
	grain3R	7.9	<2.17	51	11	57	2.83
	grain5R	8.5	<2.62	48	11	57	2.83
	grain7R	8.0	<2.37	47	11	57	2.46
	grain8R	14	<2.50	48	11	57	2.34
	grain6R	13	3.7	46	11	61	2.34
	grain10R	18	4.5	47	11	61	2.46
	grain9R	16	3.5	50	11	57	2.83
	grain11R	16	4.0	47	11	61	2.65
	grain12R	17	5.7	50	11	61	2.22
	grain14R	13	4.3	48	11	61	2.34
	grain13R	18	5.0	50	11	61	2.16
	grain15R	14	5.2	48	11	61	2.16
	grain16R	17	4.0	47	10	63	3.45
	grain17R	19	4.0	47	10	63	2.46
	grain18R	25	3.2	47	10	63	2.59
	grain19R	24	2.5	47	10	63	2.96
	grain20R	25	2.9	46	10	63	3.08
	grain2C	7.6	<2.13	48	11	57	2.28
	grain1C	13	<2.13	48	11	57	2.28
	grain4C	11	<2.09	47	11	57	2.53
	grain3C	7.8	<2.44	50	11	57	2.65
	grain5C	8.7	<1.87	48	11	57	2.65
	grain7C	9.7	<1.92	48	11	57	2.34
	grain8C	14	1.9	45	10	57	2.22
	grain6C	15	3.6	47	11	61	2.34
	grain10C	17	5.9	48	11	61	2.53

		grain9C	19	3.2	49	11	61	2.96
		grain11C	16	3.9	46	11	61	2.59
		grain12C	15	3.0	48	11	61	2.1
		grain14C	15	2.4	45	10	61	2.46
		grain13C	15	2.7	49	11	61	2.28
		grain15C	20	5.2	46	11	61	2.16
		grain16C	20	2.2	48	11	63	3.39
		grain17C	20	3.8	47	11	63	2.46
		grain18C	23	4.5	47	10	63	3.08
		grain19C	21	3.3	47	10	63	3.33
		grain20C	25	3.7	47	10	63	3.02
A12-A4-R1	Rind	grain7R	19	3.6	46	9.9	58	2.1
		grain2R	17	2.5	48	10	58	2.65
		grain3R	20	2.8	48	10	57	2.22
		grain1R	18	<3.72	50	10	55	2.53
		grain5R	21	2.9	52	10	60	2.71
		grain4R	20	<4.22	49	10	58	2.34
		grain8R	20	<2.36	51	10	60	3.14
		grain9R	18	4.4	53	11	60	2.46
		grain6R	20	<3.83	60	10	58	2.1
		grain11R	17	<1.84	51	10	60	2.65
		grain10R	16	3.2	52	10	60	2.96
		grain14R	20	3.0	47	10	56	2.77
		grain15R	14	3.3	48	10	56	2.28
		grain13R	17	4.0	49	10	58	2.46
		grain12R	24	3.1	51	10	58	2.03
		grain16R	16	4.2	51	11	58	2.46
		grain17R	23	4.8	52	10	59	2.28
		grain18R	21	2.7	52	10	59	2.4
		grain19R	19	3.0	51	9.6	59	2.28
		grain7C	19	3.2	48	10	58	2.1
		grain2C	18	<2.51	47	10	58	2.46

	grain3C	18	2.7	48	10	57	2.1
	grain1C	18	<3.86	49	10	55	1.66
	grain5C	20	<6.11	54	10	60	3.08
	grain4C	20	<1.91	51	10	58	2.59
	grain8C	22	2.7	51	10	60	2.53
	grain9C	18	6.4	48	10	60	3.2
	grain6C	21	<2.20	54	10	58	2.16
	grain11C	17	2.8	51	11	60	2.65
	grain10C	18	<2.34	52	10	60	3.02
	grain14C	22	2.8	49	10	56	2.46
	grain15C	21	3.5	49	10	57	2.1
	grain13C	22	4.1	48	10	58	2.46
	grain12C	20	2.9	52	9.9	58	1.97
	grain16C	18	3.5	49	10	58	2.28
	grain17C	21	3.2	49	11	59	2.22
	grain18C	22	4.2	50	10	59	2.46
	grain19C	21	7.2	54	11	59	2.16

Table 15: Measured and modeled δ^7Li (‰) and Li concentration (ppm) data for each traverse.

Traverse	*Variable*	*Sample Type*	*X Position (cm)*	*Measured Value*	*Calculated Value*
LA13-2	δ^7Li (‰)	Matrix	4.5	3.7	1.8
		Block	-1.7	4.0	2.6
			-2.7	4.8	2.5
			-3.7	4.2	2.5
			-4.7	2.2	2.5
	[Li] (ppm)	Matrix	4.5	68.3	20.3
		Block	-1.7	81.7	29.0
			-2.7	115.6	29.0
			-3.7	89.6	29.0
			-4.7	96.6	29.0
LA13-3	δ^7Li (‰)	Matrix	2.5	1.5	-2.8
		Block	-1.2	2.3	6.1
			-2.7	5.5	4.2
			-3.7	2.0	4.0
			-4.7	4.2	4.0
			-5.7	4.3	4.0
	[Li] (ppm)	Matrix	2.5	8.8	16.9
		Block	-1.2	69.7	39.8
			-2.7	62.6	44.9
			-3.7	52.8	45.0
			-4.7	52.4	45.0
			-5.7	44.4	45
LB13-2	δ^7Li (‰)	Matrix	4.5	-1.1	-1.3
			3.5	0.0	-1.3
			2.5	-0.8	-1.3
			2.5	-0.4	-1.3
			1.5	-0.4	-1.3
		Block	-1.8	4.6	2.2
			-2.8	5.3	1.6
			-3.8	1.4	1.5
			-4.8	3.4	1.5
	[Li] (ppm)	Matrix	4.5	9.9	16.5
			3.5	10.0	16.5
			2.5	10.7	16.5
			2.5	10.7	16.5

			1.5	8.2	16.5
		Block	-1.8	44.4	31.7
			-2.8	47.9	36.9
			-3.8	7.9	37.0
			-4.8	72.3	37.0
A10-3	δ^7Li (‰)	Block	-16.5	-3.1	-3.0
			-15.5	-1.7	-3.0
			-14.5	-1.3	-3.0
			-13.5	-1.3	-3.0
			-12.5	-4.2	-3.0
			-11.5	-2.2	-3.1
			-10.5	-2.5	-3.4
			-9.5	-3.8	-3.6
			-8.5	-1.2	-3.8
			-8.5	-2.8	-3.8
			-7.5	-2.4	-3.7
			-6.5	-1.7	-3.2
			-6.5	-2.3	-3.2
			-5.5	-1.6	-2.1
			-4.5	-0.8	-0.8
			-3.5	0.1	0.3
			-2.5	0.1	0.9
			-1.5	1.1	0.9
			-0.5	1.4	0.8
		Rind	0.5	0.3	0.6
			1.5	-0.9	0.4
			2.5	0.5	0.3
			3.5	-0.7	0.3
			4.2	0.2	0.3
			6.2	0.6	0.3
			7.2	1.1	7.2
			8.2	0.1	0.3
			9.2	1.5	0.3
			10.1	1.1	0.3
			11.1	-1.6	0.3
			13.1	-0.5	0.3
			15.1	3.4	0.3
			16.1	1.7	0.3
	[Li] (ppm)	Block	-15.5	12	12.0

			-14.5	11.2	12.0
			-13.5	10.5	12.0
			-12.5	13.4	12.0
			-11.5	10.6	12.0
			-9.5	7.5	12.1
			-8.5	11.4	12.3
			-8.5	18.6	12.3
			-7.5	10.6	12.6
			-6.5	12.3	13.1
			-6.5	0.0	13.1
			-5.5	10.7	13.7
			-4.5	11.5	14.4
			-3.5	11.4	15.1
			-2.5	12.3	15.7
			-2.5	8.3	15.7
			-1.5	13.7	16.2
			-0.5	13.3	16.3
		Rind	0.5	14.0	16.4
			1.5	11.9	16.5
			2.5	11.4	16.5
			3.5	15.8	16.5
			4.2	17.3	16.5
			6.2	15.6	16.5
			7.2	18.0	16.5
			8.2	14.1	16.5
			9.2	15.4	16.5
			11.1	21.0	16.5
			13.1	15.1	16.5
			15.1	21.4	16.5
			16.1	17.7	16.5
A12-4	δ^7Li (‰)	Block	-10.25	-4.0	-4.5
			-8.75	-4.5	-4.5
			-7.25	-5.0	-4.7
			-5.75	-6.1	-5.5
			-2.25	-0.3	0.3
			-0.75	-1.9	0.1
		Rind	0.75	-1.2	-0.4
			2.25	-0.1	-0.5
			3.75	-0.1	-0.5

			5.25	-0.9	-0.5
			6.75	0.8	-0.5
			8.25	-0.2	-0.5
			11	1.3	-0.5
	[Li] (ppm)	Block	-10.25	15.4	14.0
			-8.75	14.1	14.0
			-7.25	13.6	14.0
			-5.75	14.2	14.3
			-2.25	15.8	17.7
			-0.75	16.6	18.4
		Rind	0.75	20.4	18.5
			2.25	20.1	18.5
			3.75	18.9	18.5
			5.25	18.7	18.5
			6.75	15.3	18.5
			8.25	19.3	18.5
			11	16.4	18.5

Bibliography

Anczkiewicz, R., Platt, J. P., Thirlwall, M. F., Wakabayashi, J., 2004. Franciscan subduction off to a slow start: evidence from high-precision Lu-Hf garnet ages on high grade-blocks. *Earth and Planetary Science Letters*, **225**, 147-161.

Aulbach, S., Rudnick, McDonough, W. R. 2008. Li-Sr-Nd isotope signatures of the plume and cratonic lithospheric mantle beneath the margin of the rifted Tanzanian craton (Labait)". *Contributions to Mineralogy and Petrology*. **155** (1), 79-92.

Bebout, G. E., 2007. Metamorphic chemical geodynamics of subduction zones. *Earth and Planetary Science Letters*, **260**, 373-393.

Bebout G. E., 1997. Nitrogen isotope tracers of high-temperature fluid–rock interactions: case study of the Catalina Schist, California. *Earth and Planetary Science Letters*, **151**, 77–90.

Bebout, G.E., 1991. Field-based evidence for devolatilization in subduction zones: implications for arc magmatism. *Science*, **251**, 413–415

Bebout, G.E., and Barton, M.D., 1993. Metasomatism during subduction: products and possible paths in the Catalina Schist, California. *Chemical Geology*, **108**, 61-92.

Bebout, G. E., and Barton, M. D., 2002. Tectonic and metasomatic mixing in a high-T, subduction-zone mélange–insights into the geochemical evolution of the slab-mantle interface. *Chemical Geology*, **187**, 79-106.

Bouman, C., Elliots, T., Vroon, P.Z., 2004, Lithium inputs to subduction zones. *Chemical Geology*, **212**, 59-79.

Bickle, M. J., Chapman, H. J., Ferry, J. M., Rumble III, D., Fallick, A. E., 1997. Fluid flow and diffusion in the Waterville Limestone, south-central Maine: Constraints from strontium, oxygen and carbon isotope profiles. *Journal of Petrology,* **38**(11), 1489-1512.

Brant W.R., Schmid S., Kuhn A., Hester J., Sale, M., Gu, Q. 2012. Rapid lithium insertion and location of mobile lithium in the defect perovskite $Li_{0.18}S_{0.66}Ti_{0.5}Nb_{0.5}O_3$. *ChemPhysChem.* **13** (9), 2293-2296.

Brant, C., Coogan, L.A., Gillis, K. L., Seyfried, W. E., Pester, N. J., and Spence, J. 2012. Lithium and Li-isotopes in young altered upper oceanic crust from the East Pacific Rise. *Geochimica Et Cosmochimica Acta.* **96** (6), 272-293.

Brenan, J. M., Ryerson, F. J., Shaw, H. R., 1998a. The role of aqueous fluids in the slab-to-mantle transfer of boron, beryllium, and lithium during subduction: Experiments and models. *Geochimica et Cosmochimica Acta,* **62**, 3337-3347.

Brenan, J.M., Neroda, E., Lundstrom, C.C., Shaw, H.F., Tyerson, F.J., and Phinney, D.L., 1998b. Behaviour of boron, beryllium, and lithium during melting and crystallization: Constraints from mineral-melt partitioning experiments. *Geochimica et Cosmochimica Acta*, **62**(12), 2129-2141.

Bryant, C. J., Chappell, B. W., Bennett, V. C., McCulloch, M. T. 2004. Lithium isotopic compositions of the New England Batholith: correlations with inferred source rock compositions. *Transactions of the Royal Society of Edinburgh: Earth Sciences.* **95** (1-2), 1-2.

Caciagli, N., Brenan, J. M., McDonough, W. F., Phinney, D., 2011, Mineral-fluid partitioning of lithium and implications for slab-mantle interaction. *Chemical Geology*, **280**, 384-398.

Chan, L. H., Alt, J. C., Teagle, D. A. H., 2002, Lithium and lithium isotope profiles through the upper oceanic crust: a study of seawater-basalt exchange at ODP Sites 504B and 896A. *Earth and Planetary Science Letters*, **201**, 187-201.

Chan, L., Leeman, W. P., Plank, T., 2006, Lithium isotopic composition of marine sediments. *Geochem. Geophys. Geosys.*, **7**, 6.

Chan, L. H., Edmond, J. M., Thompson, G., Gillis, K., 1992, Lithium isotopic composition of submarine basalts: implications for the lithium cycle in the oceans. *Earth and Planetary Science Letters*, **108**, 151-160.

Chan, L.-H. and Frey, F. A. 2003. Lithium isotope geochemistry of the Hawaiian plume: Results from the Hawaii Scientific Drilling Project and Koolau Volcano.*Geochemistry, Geophysics, Geosystems.* **4** (3).

Davis, A. M., MacPherson, G. J., Clayton, R. N., Mayeda, T. K., Sylvester, P. J., Grossman, L., Hinton, R. W., and Laughlin, J. R., 1991. Melt solidification and late-stage evaporation in the evolution of a FUN inclusion from the Vigarano C3V chondrite. *Geochimica et Cosmochimica Acta,* **55,** 621–637.

Dutrow, B.L., Holdaway, M.J., and Hinton, R.W., 1986. Lithium in staurolite and its petrologic significance. *Contributions to Mineralogy and Petrology*, **94**, 496-506.

Elliott, T., 2003. Tracers of the slab. In: Eiler, J. (Ed.), Inside the Subduction Factory. *American Geophysical Union, Geophysical Monogram*, **138**, 23–45.\

Elliott, T., Thomas, A., Jeffcoate, A., and Niu, Y. 2006. Lithium isotope evidence for subduction-enriched mantle in the source of mid-ocean-ridge basalts.*Nature*. **443** (7111), 565.

Gao,Y., Casey, J.F., 2011. Lithium isotope composition of ultramafic geological reference materials: JP-1 and DTS-2. *Geostandards and Geoanalytical Research.* **36**(1), 75-81.

Genske, F.S., Turner, S. P., Beier, C., Chu, M. F., Tonarini, S., Pearson, N. J., and Haase, K.M. 2014. Lithium and boron isotope systematics in lavas from the Azores islands reveal crustal assimilation. *Chemical Geology*. **373,** 27-36.

Gorman, Julia, 2013. The role of mechanical mixing in the formation of reaction zones in subduction-related melange, University of Maryland, MS thesis, http://hdl.handle.net/1903/14504.

Grove, M., Bebout, G. E., Jacobson, C. E., Barth, A. P., Kimbrough, D. L., King, R. L., Zou, H., Lovera, O. M., Mahoney, B. J., Gehrels, G. E., 2008, The Catalina Schist: Evidence for Mid-Cretaceous Subduction Erosion of southwester North America. *Geological Society of America Special Paper*, **436**, 335-361.

Halama, R., McDonough, W. F., Rudnick, R. L., Keller, J., Klaudius, J., 2007, The lithium isotopic composition of Oldoinyo Lengai: Nature of the mantle sources and lack of isotopic fractionation during carbonatite petrogenesis. *Earth and Planetary Science Letters*, **254** (1), 77-89.

Halama, R., Mcdonough, W. F., Rudnick, R. L., Bell, K., 2008, Tracking the lithium isotopic evolution of the mantle using carbonatites. *Earth and Planetary Science Letters*, **265** (3), 726-742.

Halama, R., Savov, I. P., Rudnick, R. L., McDonough, W. F., 2009. Insights into Li and Li isotope cycling and sub-arc metasomatism from veined mantle xenoliths, Kamchatka. *Contributions to Mineral Petrology*, **158**, 197-222.

Halama, R., John, T., Herms, P., Hauff, F., and Schenk, V. 2011. A stable (Li, O) and radiogenic (Sr, Nd) isotope perspective on metasomatic processes in a subducting slab.*Chemical Geology.* **281**(3-4), 151-166.

Hawthorne, F. C., Ungaretti, L., Oberti, R., Caucia, F., and Callegari, A., 1993. The crystal chemistry of staurolite. I. Crystal structure and site populations. *the Canadian Mineralogist*, **31**, 551-582.

Hoefs, J., 1997. Stable Isotope Geochemistry, 4th ed. xi + 200 pp. Berlin, Heidelberg, New York, London, Paris, Tokyo, Hong Kong: Springer-Verlag. ISBN 3 540 61126 6.

Jackson, S. E., 2008. LAMTRACE data reduction software for LA–ICP–MS, in *Laser ablation ICP–MS in the earth sciences: current practices and outstanding issues* (ed. P. Sylvester), 305–307, Short Course Series, 40, Mineralogical Association of Canada,Québec.

James, R. H., and Palmer, M. R. 2000. The lithium isotope composition of international rock standards. *Chemical Geology.* **166** (3-4), 319-326.

Jeffcoate, A., B., Elliott, T., Thomas, A., Bouman, C., 2004. Precise/ Small Sample Size Determinations of Lithium Isotopic compositions of Geological Reference Materials and Modern Seawater by MC-ICP-MS. *Geostandards and Geoanalytical Research*, **28**(1), 161-172.

Jeffcoate, A. B., Elliott, T., Kasemann, S.A., Ionov, D., Cooper, K., Brooker, R., 2007, Li isotope fractionation in peridotites and mafic melts. *Geochimica et Cosmochimica Acta*, **71**, 202-218.

Jochum, K. P., Stoll, B., Herwig, K., Willbold, M., Hofmann, A. W., Amini, M., Aarburg, S., ... Woodhead, J. D. 2006. MPI-DING reference glasses for in situ microanalysis: New reference values for element concentrations and isotope ratios. *Geochemistry, Geophysics, Geosystems*, **7**, *(*2).

John, T., Gussone, N, Podladchikov, Y.Y., Bebout, G. E., Dohmen, R., Halama, R., Klemd, R, Magna, T., Seitz, H. M., 2012, Volcanic arcs fed by rapid pulsed fluid flow through subducting slabs. *Nature Geoscience*, **5**, 489-492.

Kasemann, S. A., Jeffcoate, A. B., Elliott, T., 2005. Lithium isotope composition of basalt glass reference material. *Analytical Chemistry*, **77**(16), 5251-5257.

Krienitz M.-S., Garbe-schonberg C.-D., Romer R.L., Meixner A., Stroncik N.A., and Haase K.M. 2012. Lithium isotope variations in ocean Island Basalts-implications for the development of mantle heterogeneity. *Journal of Petrology.* **53** (11), 2333-2347.

Liu, X. M., Rudnick, R. L., Hier-Majumder, S., 2010, Processes controlling lithium isotopic distribution in contact aureoles: A case study of the Florence County pegmatites, Wisconsin. *Geochemistry Geophysics Geosystems*, **11**(8), 1-21.

Liu, X.M., Rudnick, R. L., McDonough, W. F., Cummings, M. L. 2013. Influence of chemical weathering on the composition of the continental crust: Insights from Li and Nd isotopes in bauxite profiles developed on Columbia River Basalts. *Geochimica et Cosmochimica Acta, **115,*** 73-91.

Liu, X-M., Wanner, C., Rudnick, R. L., McDonough, W. F., In Press. Processes controlling δ^7Li in rivers illuminated by study of streams and ground waters draining basalts. *Earth and Planetary Science Letters.*

Magna, T., Wiechert, U. H., Halliday, A. N., 2004. Low-blank isotope ratio measurement of small samples of lithium using multiple-collector ICPMS. *International Journal of Mass Spectrometry*, **239**, 67-76.

Magna, T., Wiechert, U., Grove, T. L., Halliday, A. N. 2006a. Lithium isotope fractionation in the southern Cascadia subduction zone. *Earth and Planetary Science Letters.* **250**(3-4), 428-443.

Magna, T., Wiechert, U., Halliday, A. N. 2006b. New constraints on the lithium isotope compositions of the Moon and terrestrial planets. *Earth and Planetary Science Letters.* **243**(3-4), 336-353.

Magna, T., Simcikova, M., Moynier, F. 2014. Lithium systematics in howardite-eucrite-diogenite meteorites: Implications for crust-mantle evolution of planetary embryos. *Geochimica Et Cosmochimica Acta.* **125**, 131-145.

Maloney, J. S., Nabele, P. I., Sirbescu, M.-L. C., Halama, R., 2008, Lithium and its isotopes in tourmaline as indicators of the crystallization process in the San Diego County pegmatites, California, USA. *European Journal of Mineralogy*, **20** (5), 905-916.

Marschall, H. R., Pogge von Strandmann, P.A.E., Seitz, H.-M., Elliott, T., Niu, Y. 2007. The lithium isotopic composition of orogenic eclogites and deep subducted slabs. *Earth and Planetary Science Letters.* **262** (3), 563-580.

Marks, M. A. W., Rudnick, R. L., Ludwig, T., Marschall, H., Zack, T., Halama, R. McDonough, W. F., Rost, D., Wenzel, T., Vicenzi, E. P., Savov, I., P., Altherr, R., Markl, G., 2008, Sodic pyroxene and sodic amphibole as potential reference materials for *in situ* lithium isotope determinations by SIMS. *Geostandards and Geoanalytical Research*, **32** (3), 295-310.

Millot, R., Guerrot, C., Vigier, N., 2004, Accurate and high-precision measurement of lithium isotopes in two reference materials by MC-ICP-MS. *Geostandards and Geoanalytical Research*, **28** (1), 153-160.

Morris, J.D., Ryan, J.G., 2003, Subduction zone processes and implications for changing composition of the upper and lower mantle. *Treatise on Geochemistry*, **2**, 451–470.

Oi, T., Nomura, M., Musashi, M., Ossaka, T., Okamoto, M., and Kakihana, H., 1989. Boron isotopic composition of some boron minerals, *Geochimica et Cosmochimica Acta*, **53**, 3189-3195.

Ottolini, L., Laporte, D., Raffone, N., Devidal, J.L., Le Févre, B., 2009, New experimental determination of Li and B partition coefficients during upper mantle partial melting. *Contributions to Mineral Petrology*, **157**, 313-325.

Penniston-Dorland, S. C., Ferry, J. M., 2008. Element mobility and scale of mass transport in the formation of quartz veins during regional metamorphism of the Waits River Formation, east-central Vermont. *American Mineralogist.* **93** (1), 7-21.

Penniston-Dorland, S.C., Sorensen, S.S., Ash, R.D., Khadke, S.V. 2010. Lithium isotopes as a tracer of fluids in a subduction zone melange: Franciscan Complex, CA. *Earth and Planetary Science Letters.* **292** (1-2), 181-190.

Penniston-Dorland, S. C., Bebout, G. E., Pogge von Standmann, P. A. E., Elliott, T., Sorensen, S. S., 2012a, Lithium and its isotopes as tracers of subduction zone fluids and metasomatic processes: Evidence from the Catalina Schist, Califoria, USA. *Geochimica et Cosmochimica Acta*, **77**, 530-545.

Penniston-Dorland, S.C., Walker, R. J., Pitcher, L., Sorensen, S. S., 2012b, Mantle-crust interactions in a paleosubduction zone: Evidence from highly siderophile element systematics of eclogite and related rocks. *Earth and Planetary Science Letters*, **319**, 295-306.

Penniston-Dorland, S.C., Gorman, J.K., Bebout, G.E., Piccoli, P.M., and Walker, R.J., 2014. Reaction rind formation in the Catalina Schist: Deciphering a history of mechanical mixing and metasomatic alteration. *Chemical Geology*. **384**, 47-61.

Pistiner, J. S., and Henderson, G. M. 2003. Lithium-isotope fractionation during continental weathering processes. *Earth and Planetary Science Letters*, **214** (1-2), 327-339.

Platt, J. P., 1975, Metamorphic and deformation processes in the Franciscan Complex, California: Some insights from the Catalina Schist terrane. *Geological Society of America Bulletin*, **86**, 1337-1347.

Qiu, L., Rudnick, R. L., McDonough, W. F., Merriman, R. J., 2009, Li and δ^7Li in mudrocks from the British Caledonides: Metamorphism and source influences. *Geochimica et Cosmochimica Acta*, **73**, 7325-7340.

Richter, F. M., Davis, A. M., DePaolo, D. J., Watson, E. B., 2003, Isotope fractionation by chemical diffusion between molten basalt and rhyolite. *Geochimica et Cosmochimia Acta*, **67**, 3905-3923.

Richter, F.M., Mendybaev, R.A., Christensen, J.N., Hutcheon, I.D., Williams, R.W., Sturchio, N.C., Beloso Jr., A.D., 2006, Kinetic isotopic fractionation during diffusion of ionic species in water. *Geochimica et Cosmochimica Acta*, **70**, 277–289.

Richter, F. M., Watson, B., Chaussidon, M., Mendybaev, R., Ruscitto., D., 2014, Lithium isotope fractionation by diffusion in minerals. Part 1: Pyroxenes. *Geochimica et Cosmochimica Acta*, **126**, 352-370.

Rosner, Martin, Ball, L., Peucker-Ehrenbrink, B., Blusztajn, J., Bach, W., Erzinger, J. 2007. A Simplified, Accurate and Fast Method for Lithium Isotope Analysis of Rocks and Fluids, and δ^7Li Values of Seawater and Rock Reference Materials. *Geostandards and Geoanalytical Research.* **31** (2), 77-88.

Rudnick, R. L., Tomascak, P. B., Njo, H. B., Gardner, R. L., 2004, Extreme lithium isotopic fractionation during continental weathering revealed in saprolites from South Carolina. *Chemical Geology*, **212**, 45-58.

Rudnick, R. L. and Ionov, D. A., 2007, Lithium elemental and isotopic disequilibrium in minerals from peridotite xenoliths from far-east Russia: Product of recent

melt/fluid-rock reaction. *Earth and Planetary Science Letters*, **256** (1), 278-293.

Schuessler, J. A., Schoenberg, R., Sigmarsson, O., 2009. Iron and lithium isotope systematics of the Hekla volcano, Iceland – Evidence for Fe isotope fractionation during magma differentiation. *Chemical Geology*. **258**, 78-91.

Sorensen, S. S., 1986, Petrologic and geochemical comparison of the blueschist and greenschist units of the Catalina Schist terrane, southern California. *Geological Society of America, Memoir*, **164**, 59-75.

Sorensen, S.S., 1988, Petrology of amphibolite-facies mafic and ultramafic rocks from the Catalina Schist, Southern California; metasomatism and migmatization in a subduction zone metamorphic setting. *Journal of Metamorphic Geology*, **6**, 405-435.

Sorensen, S.S. and Barton, M.D., 1987, Metasomatism and partial melting in a subduction complex: Catalina Schist, southern California. *Geology*, **15**, 115-118.

Sorensen, S. S. and Grossman, J. N., 1989, Enrichment of trace elements in garnet amphibolites from a paleo-subduction zone: Catalina Schist, southern California. *Geochimica et Cosmochimica Acta*, **53**, 3155-3178.

Suppe, J., Armstrong, R. L., 1972, Potassium-Argon dating of Franciscan metamorphic rocks. *American Journal of Science*, **272**, 217-233.

Tatsumi, Y., 2005, The subduction factory: how it operates in the evolving Earth. *GSA Today*, **15**, 4–10.

Taylor, I.T. and Urey, H.C.,1928. Fractionation of lithium and potassium isotopes by chemical exchange with zeolite. *Journal of Chemical Physics*, **6**, 429-438.

Teng, F-Z., McDonough, W.F., Rudnick, R.L., Dalpé, C., Tomascak, P.B., Chappell, B.W. and Gao, S., 2004, Lithium isotopic composition and concentration of the upper continental crust. *Geochimica et Cosmochimica Acta*, **68,** 4,167-4,178.

Teng, F-Z., McDonough, W.F., Rudnick, R.L., Walker, R.J., 2006. Diffusion-driven extreme lithium isotopic fractionation in country rocks of the Tin Mountain pegmatite. *Earth and Planetary Science Letters*, **243**, 701-710.

Teng, F-Z., McDonough, W. F., Rudnick, R. L., Wing, B. A., 2007, Limited lithium isotopic fractionation during progressive metamorphic dehydration in metapelites: A case study from the Onawa contact aureole, Maine. C*hemical Geology*, **239** (1), 1-12.

Tian, S., Hou, Z., Su, A., Hou, K., Hu, W., Li, Z., Zhao, Y., Gao, Y., Li, Y., Yang, D., Yang, Z. 2012. Separation and Precise Measurement of Lithium Isotopes in Three Reference Materials Using Multi Collector-Inductively Coupled Plasma Mass Spectrometry. *Acta Geologica Sinica - English Edition.* **86** (5), 1297-1305.

Tomascak, P. B., Langmuir, C. H., le Roux, P. J., Shirey, S. B., 2008, Lithium isotopes in global mid-ocean ridge basalts. *Geochimica et Cosmochimica Acta*, **72**, 1626-1637.

Wegner, M., Armbruster, T., and Geiger, C., 1991. Cation distribution in partially ordered columbite from the Kings Mountain pegmatite, North Carolina. *American Mineralogist*, **76**, 1897-1904.

Wunder, B., Meixner, A., Romer, R.L., Heinrich, W., 2006. Temperature-dependent isotopic fractionation of lithium between clinopyroxene and high-pressure hydrous fluids. *Contributions to Mineral Petrology*, **151**, 112-120.

Wunder, B., Meixner, A., Romer, R. L., Feenstra, A., Schettler, G., Heinrich, W., 2007. Lithium isotope fractionation between Li-bearing staurolite, Li-mica and aqueous fluids: An experimental study. *Chemical Geology*, **238**, 277-290.

Wunder, B., Meixner, A., Romer, R. L., Jahn, S., 2011. Li-isotope fractionation between silicates and fluids: Pressure dependence and influence of the bonding environment. *European Journal of Mineralogy*, **23**, 333-342.

Yamaji, K., Makita, Y., Watanabe, H., Sonoda, A., Kanoh, H., Hirotsu, T., and Ooi, K., 2000. Theoretical estimation of lithium isotopic reduced partition function ratio for lithium ions in aqueous solution. *Journal of Physical Chemistry*, **105**, 602-613.

Zack, T., Tomascak, P. B., Rudnick, R. L., Dalpé, C., McDonough, W. F., 2003, Extremely light Li in orogenic eclogites: The role of isotope fractionation during dehydration in subducted oceanic crust. *Earth and Planetary Science Letters*, **208**, 279-290.